JOSE E. RANGEL

Supervisor: YANYAN SHA

Dropped Object Impact on GFRP Molded Gratings for Subsea Pipeline Protection: A Study on Optimizing for Impact Energy Absorption

Master thesis, 2024

MSc. in Mechanical and Structural Engineering

Faculty of Science and Technology

Department of Mechanical and Structural Engineering and Materials Science

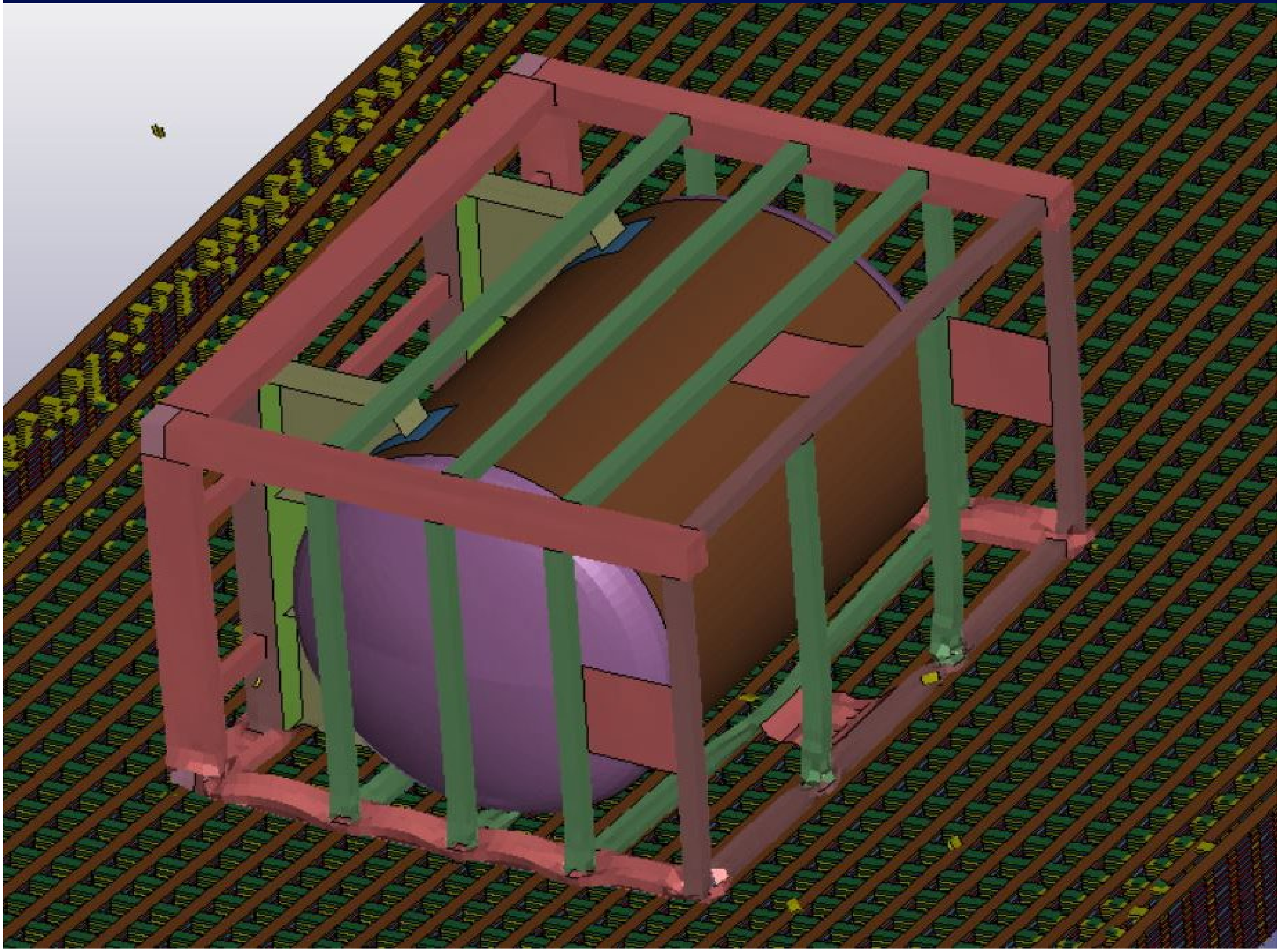

Abstract

Subsea pipelines must be protected against external loads that could cause excessive damage and lead to hydrocarbon release, such as impact loads from dropped objects. Glass Fiber-Reinforced Plastic (GFRP) for protection against impact loads has gained popularity due to its good energy absorption capacity, superior strength-to-weight ratio, and cost-effectiveness compared to other materials.

GFRP molded gratings have high bidirectional stiffness and effectively redistribute concentrated loads, such as impacts from dropped objects. However, limited literature exists on their energy absorption capacity and ability to protect subsea pipelines against dropped objects.

This thesis investigates the ability of GFRP gratings to dissipate sufficient energy from dropped objects to avoid risk of hydrocarbon release from the pipeline. In this research, Non-Linear Finite Element Analysis (NLFEA) using LS-DYNA was employed to assess the energy absorption capacity of GFRP molded gratings under different impact scenarios involving a tank with a kinetic energy of 99.1 kJ, modeled as both rigid and deformable body.

The Multi-objective Optimization Genetic Algorithm (MOGA) was used to optimize the dimensions of the GFRP grating for energy absorption. The results from the optimization model indicated that a grating with dimensions of 7.9x62.7x22.4 mm (WxHxP) provides the best balance between impact energy dissipated and cost.

Key findings reveal that the grating thickness significantly influences the impact resistance and energy absorption capacity of GFRP molded gratings. The grating geometries studied in this paper completely lose structural integrity upon impact and fail to dissipate the total kinetic energy from the dropped object. However, the impact resistance can be enhanced by designing substructures that integrate GFRP gratings with stiffeners connected beneath the grating, acting as reinforcement and increasing the total impact energy dissipated.

This study establishes a foundation for understanding the parameters affecting the energy absorption capacity of GFRP gratings, providing insights for future research and practical applications in subsea pipeline protection.

Acknowledgments

I want to express my most sincere gratitude to all those who have supported me throughout my journey to complete this thesis.

First, I want to thank my **mother, Leisy Revett**, for her unconditional support during my academic journey. Her encouragement and belief in me have been my greatest source of strength.

I am deeply grateful to my **family** for their economic and emotional support throughout my master's degree.

I want to thank Professor **Yanyan Sha** for being my supervisor and guiding me through this research. His expertise and insights on troubleshooting convergence issues with the FEA models have been invaluable.

I extend my gratitude to **Dynamore Nordic AB** for providing training in LS-DYNA and offering continuous support with modeling and convergence challenges during the simulations.

I would also like to thank **Alejandro Graterol** for providing valuable insights into using the genetic algorithm for optimization problems, which significantly enhanced the quality of this research.

I am also thankful to **Glassfiber Produkter AS** for sharing information regarding the manufacturing of GFRP molded gratings and their energy absorption capacity under dropped object impact. This collaboration has been key in the practical aspects of this thesis.

The simulations in this study were performed on the resources provided by **Sigma2, the National Infrastructure for High-Performance Computing and Data Storage in Norway (project number NN9721K). We gratefully acknowledge this support**.

Thank you all for your support and contributions to my academic journey.

Table of Contents

1 List of Figures VI
2 List of Tables VIII
1 Introduction 1
  1.1 Motivation 1
  1.2 Limitations and challenges 1
2 Background 3
  2.1 Previous work on dropped object impact analysis 3
  2.2 Subsea pipeline protection systems 4
  2.3 GFRP molded gratings 5
  2.4 Applicable standards 7
    2.4.1 DNVGL -RP-C204 7
    2.4.2 DNVGL RP-F-107 8
3 Methodology 10
  3.1 FEM for analysis of non-linear dynamic systems 10
    3.1.1 Explicit solvers 11
  3.2 Tools 12
    3.2.1 LS-DYNA 12
    3.2.2 High-Performance Computing (HPC) 12
    3.2.3 MATLAB 12
  3.3 Geometries 13
    3.3.1 Dropped object 13
    3.3.2 Protective cover 14
  3.4 GFRP mechanical properties 15
    3.4.1 Longitudinal mechanical properties 17
    3.4.2 Transverse mechanical properties 18
  3.5 GFRP energy absorption 19
  3.6 Material damage models 20
    3.6.1 MAT054 20
    3.6.2 MAT024 21
  3.7 FEA Numerical modeling 22

3.7.1 Contact formulations and element type 22
3.7.2 Boundary conditions 23
3.8 Structural optimization 23
3.8.1 Design of Experiments (DoE) and Response Surface Methodology (RSM) .. 24
3.8.2 Genetic Algorithm (GA) optimization 25
4 Model validation 26
4.1 Material model verification 26
4.2 Discussion on convergence 28
4.2.1 Mesh 28
4.2.2 Energy balance 29
4.2.3 Hourglass 30
4.3 Boundary conditions 30
4.3.1 Tank scaling 31
5 Analysis and results 33
5.1 Impact scenarios 33
5.2 Rigid tank impact 34
5.2.1 Analysis of impact scenarios 34
5.2.2 Design of Experiments (DoE) 35
5.2.3 Strain energy 35
5.2.4 Energy balance and hourglass 37
5.3 Grating size optimization 38
5.3.1 Response Surface Methodology (RSM) 38
5.3.2 MOGA optimization 40
5.3.3 Discussion on model accuracy 41
5.4 Deformable tank impact 42
5.4.1 Flat impact 42
5.4.2 Tip-side impact 44
5.4.3 Analysis of impact scenarios 45
5.4.4 Energy balance and hourglass 46
5.5 Additional simulations 47
5.5.1 Energy absorption capacity 47
5.5.2 Local reinforcements 49
6 Conclusion 51

7 Further work and improvements 52
8 References 53
9 Appendix 56
Appendix A: NLFEA Simulation data 56
Appendix A.1: Simulation workflow for dropped object impact analysis on GFRP gratings 56
Appendix A.2: LS-DYNA material card of the molded grating reinforced laminae 57
Appendix A.3: LS-DYNA material card of the molded grating unreinforced laminae .. 58
Appendix A.4: LS-DYNA material card of steel S355 with modified dynamic yielding 58
Appendix B: Simulation Results 59
Appendix B.1: Deformable tank flat impact simulation 59
Appendix B.1.1: Original thickness. Effective plastic strain after GFRP integrity loss 59
Appendix B.1.2: Original thickness. Von misses stress distribution of the scaled tank after GFRP integrity loss 59
Appendix B.1.3: Reduced thickness. Von misses stress distribution of the scaled tank after GFRP integrity loss 60
Appendix B.2: Deformable tank tip side impact simulation 61
Appendix B.2.1: Original thickness. Effective plastic of the tank until progressive damage initiation in GFRP 61
Appendix B.2.2: Original thickness. Von misses stress distribution of the tank until progressive damage initiation in GFRP 61
Appendix B.2.3: Increased thickness. Von misses stress distribution of the tank until progressive damage initiation in GFRP 62
Appendix B.2.4: Increased thickness. Von misses stress distribution of the scaled tank after GFRP integrity loss 62
Appendix B.3: Beam-reinforced grating. Von Misses stress distribution of the steel components 63
Appendix B.4: Response Surface Methodology (RSM) results 64
Appendix B.4.1: Response surface - Influence of mass and fiber volume fraction 64
Appendix B.4.2: Response surface - Influence of grid pitch and rib thickness. 64
Appendix B.4.3: Response surface - Influence of grid pitch and grating thickness. ... 65

1 List of Figures

Figure 1. Three stages of dropping objects process (Obtained from Xiang G. et al. [4]). 3
Figure 2. Concrete mattress for pipeline protection (Obtained from Shoretec [11]). 4
Figure 3. Cover dimensions for a 1m diameter pipeline (Obtained from Tauqueer M. et al. [12]). 5
Figure 4. Illustration of implementation of FRP gratings for subsea equipment protection (Obtained from PJNC Ltd UK [14]). 6
Figure 5. The general structure of a GFRP molded grating (Reproduced from Gattesco et al. [15]). 6
Figure 6. Absorption of dropped object kinetic energy as strain energy in the installation (Obtained from DNV RP-C204 [16]). 8
Figure 7. Dimensions of the tank frame from: top view (A), front view (B), side view (C), and only tank front view (D). All dimensions are in meters. 14
Figure 8. Conceptual design of the tunnel structure: Isometric view (left) and front view (right). All dimensions are in meters. 15
Figure 9. Characteristic dimensions of GFRP molded gratings. 15
Figure 10. Laminate ply axes (Obtained from Research Lewis Center [24]) 17
Figure 11. Flowchart for NLFEA simulation of dropped object impact in LS-DYNA. 22
Figure 12. FEA model of 3-point bending test. 26
Figure 13. Force vs displacement curves for each study. 28
Figure 14. Adjusted domain after tank scaling. 29
Figure 15. 4 out of 12 total hourglass modes of an eight-node cubic element (Obtained from LS-DYNA theory manual [21]). 30
Figure 16. Stress distribution near the extended longitudinal boundaries. 31
Figure 17. Stress-strain curve for steel S355 (original and scaled tank). 32
Figure 18. Impact scenarios (front view): flat (E), tip (F), side tip (G). 33
Figure 19. Grating test No. 4: effective plastic strain distribution 0.034 s after initial impact (left) and total energy absorbed (right). 36
Figure 20. Rigid tank: test grating No. 4 total energy. 37
Figure 21. Goodness of fit for the Kriging model. 38
Figure 22. Sensitivity analysis of geometric variables: 20% increase (left), 20% decrease (right). 40
Figure 23. Mutated grating candidates after performing MOGA. 41
Figure 24. Total energy dissipation after impact on optimized grating geometry. 42
Figure 25. Deformable tank flat impact: contact force vs time. 43
Figure 26 Total energy dissipation after impact: original scaled wall thickness (left) and reduced wall thickness (right). 44
Figure 27 Total energy dissipation after impact: original scaled wall thickness (left) and increased wall thickness (right). 45
Figure 28 Comparison of deformable tank impact scenarios. 46
Figure 29. Deformable tank model total energy. 46
Figure 30 Effective plastic strain in GFRP upon bounce-back. 48

Figure 31 Rigid surge tank impact: energy dissipated (left) and force vs indentation (right). 48
Figure 32. Effective plastic strain of the beam-reinforced GFRP molded grating. 49
Figure 33 Internal energy component breakdown (left) and total energy dissipated (right). 50

2 List of Tables

Table 1. Sections of the tank and frame. 13
Table 2. Mechanical properties of base materials of GFRP gratings [13]......................... 16
Table 3. Boundary conditions. 23
Table 4. 3-point bending test setup. 26
Table 5. Comparison of quasi-static bending numerical simulations................................ 27
Table 6. Energy absorbed by the GFRP grating in different impact scenarios with a rigid tank. 34
Table 7. Upper and lower bounds of GFRP grating geometric variables........................... 34
Table 8. Geometries generated from the CCD. 35
Table 9. Mesh metrics for test grating No.4. 36
Table 10. Metrics of the regression model. 39
Table 11. Top candidates obtained from the optimization model....................................... 41
Table 12. Flat impact. total strain energy per component. 43
Table 13. Side tip impact. total strain energy per component. 44

1 Introduction

Subsea pipelines are vital in oil and gas operations, allowing safe and efficient transport of hydrocarbons. However, they are susceptible to unexpected external loads, which can cause excessive damage to the pipeline and hydrocarbon release to the marine environment. To mitigate these risks, it is essential to account for accidental load cases, such as dropped object impact, and to design robust protective structures accordingly.

This thesis aims to investigate the ability of Glass Fiber-Reinforced Plastic (GFRP) molded gratings to protect subsea pipelines from dropped objects with kinetic energies that pose a high risk of hydrocarbon release. By using Non-Linear Finite Element Analysis (NLFEA), this work intends to provide a comprehensive study of the energy absorption capacity of GFRP molded gratings under different impact scenarios and analyze the critical geometric parameters that affect their ability to absorb energy from the dropped object.

This research aims to improve the understanding of GFRP gratings performance under impact loads and assess its potential for pipeline protection. The findings are expected to address a notable gap in the existing peer-reviewed literature.

1.1 Motivation

GFRP covers are increasingly popular due to their higher strength-to-weight ratio and lower costs compared to other materials [1]. In addition to their excellent mechanical performance, they possess good energy absorption behavior [1]. While Fiber Reinforced Plastic (FRP) is used alone or in combination with other materials for impact protection in offshore structures [2], there is limited peer-reviewed literature studying their energy absorption capacity after impact from dropping objects and their suitability for protecting subsea pipelines.

Since GFRP molded gratings are marketed as a suitable solution for reinforcing structures and protecting subsea equipment against dropped object impacts [3], this work is motivated by the need to explore their capabilities for subsea pipeline protection

1.2 Limitations and challenges

Several limitations were encountered while setting up the NLFEA simulations. Modeling penetrating/contacting bodies and non-linear material required non-linear solvers. Additionally, modeling the progressive failure of the GFRP gratings required solid elements. As a result, the finite element model was highly complex, requiring a significant amount of computing power to solve.

There is always a trade-off between the accuracy of the solution and the computational resources available. Although the University of Stavanger (UiS) had access to a High-Performance Cluster (HPC) with substantial computing power, the total number of computing hours allocated for the project was restricted. Therefore, it was necessary to simplify the problem domain to set up a simulation that could be solved within the available resources while still accurately representing the physical behavior of the GFRP gratings under impact loading.

Explicit dynamic simulations, commonly used to model object impact, rely on factors such as contact modeling complexity and the minimum timestep automatically set by LS-DYNA based on the smallest element size. As the elements deform, the timestep can decrease significantly if a distorted element reduces in volume, extending the initially estimated solution time. This was a significant issue experienced while running simulations on the HPC, as several computing hours were consumed before the simulation was error terminated or the solid volume element was excessively reduced.

Troubleshooting simulation termination errors was also challenging, as these errors could arise from various factors, including contact formulation, element size, initial penetration, and numerical instabilities. Consequently, during the initial stages of the study, a substantial amount of computing hours was spent refining the material model of the GFRP gratings, reducing the resources available for more complex simulations performed at later stages of this research.

Toward the end of the project, simulations had to be performed on workstations with a maximum computing capacity of 8 cores, as all the allocated HPC hours were consumed testing different gratings sizes to develop the response surface. The use of solid elements led to high computational costs. Hence, some simulations took approximately 60 hours on 8 cores to solve when using under-integrated elements. The computation time doubled when using fully integrated elements and tripled when modeling the tank as a deformable object. This limitation resulted in fewer tests than desired to characterize the GFRP molded grating energy absorption capacity.

2 Background

2.1 Previous work on dropped object impact analysis

Previous research has been conducted to study the damage of dropping objects on subsea structures and pipelines. Xiang G. et al. [4] researched methodologies for risk assessment of dropped objects from marine operations on subsea structures and evaluated the changes in dropped object trajectories from the free surface to the seabed (See Figure 1), proposing an update to the object excursion and risk probability rings methodology on DNVGL RP F-107 [5].

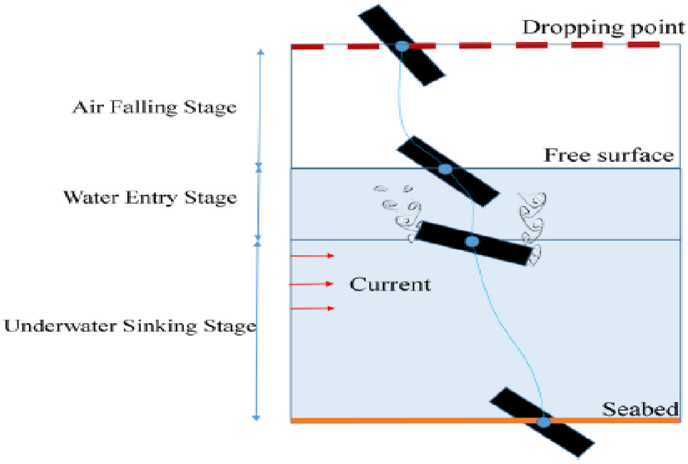

Figure 1. Three stages of dropping objects process (Obtained from Xiang G. et al. [4]).

Additionally, the Dropped Object Prevention Scheme (DROPS) has performed a quantitative assessment of the total impact energy of various common subsea-dropped objects [6], identifying an approximated spectrum of the impact energies likely to cause pipeline damage and hydrocarbon release.

Furthermore, Wenger et al. [2] have done experimental research on the parameters affecting the design of impacted structures, providing insights into the response of stiffened plates and hatch covers under the impact of collar drills.

Given the complexities of full-scale impact testing and the recent technological developments in Finite Element Analysis (FEA) software, numerous studies explore using NLFEA software to investigate post-impact energy absorption of subsea pipelines and structures. Contrary to the common practice of treating dropped objects as infinitely rigid bodies in FEA simulations, both Zhenhui Liu [7] and Ramberg Amalie [8] have found that this approach leads to an underestimation in total energy absorbed, highlighting that treating the dropping object as a deformable object can increase the total energy dissipation.

2.2 Subsea pipeline protection systems

The engineering of subsea pipeline protection systems requires materials with good energy absorption capabilities to dissipate energy from dropped objects and avoid pipeline damage. Several materials that meet these requirements, such as concrete, FRP, steel, and aluminum, are used for subsea equipment protection systems [2].

There are various options available in the market for pipeline protection. Concrete mattresses and FRP are among the solutions offered by several engineering companies specializing in subsea equipment protection.

Concrete mattresses provide a recognized engineering solution for the challenges faced in subsea pipeline construction [9]. Typically, concrete mattresses may be used to, among other things, protect the pipeline from dropped object impact. Protection is provided by mattresses, consisting of concrete blocks connected by steel or synthetic material. The concrete blocks are covered with special pads to prevent the pipeline from being damaged [10]. For reference, Figure 2 shows a drawing of a typical concrete mattress used for pipeline protection.

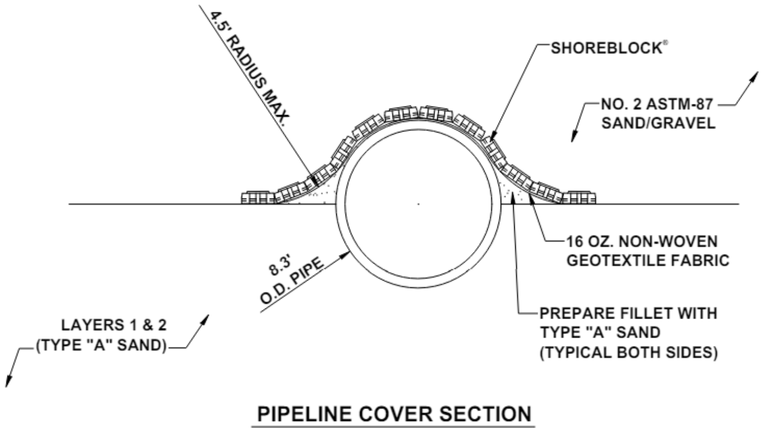

Figure 2. Concrete mattress for pipeline protection (Obtained from Shoretec [11]).

As previously mentioned, GFRP is also a suitable solution for pipeline protection covers. In this regard, Tauqueer M. et al. [12] have directly studied how the geometry of GFRP protective covers affects impact energy absorption and its suitability for protection against different impact energies from rigid objects. They analyzed GFRP plates with square, triangular, and semi-circular shapes (see Figure 3). Their findings indicated that the GFRP protection covers have an impact absorption capacity of the order of impact energies of the dropped objects released from fishing activities [12], which is approximately 15 kJ.

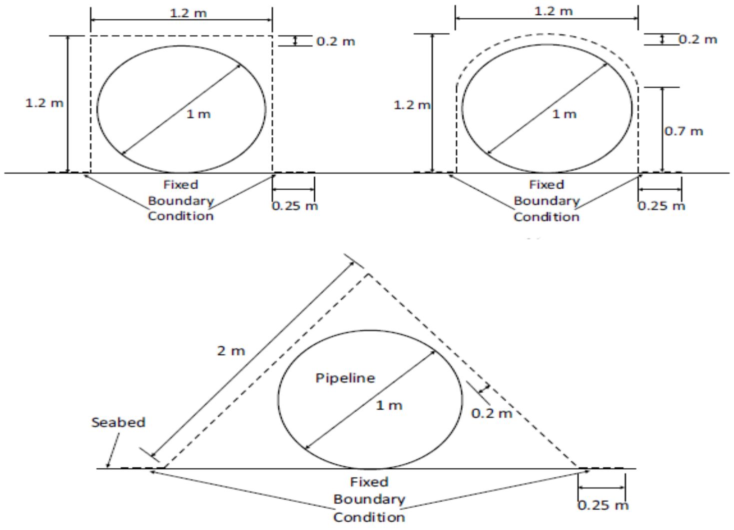

Figure 3. Cover dimensions for a 1m diameter pipeline (Obtained from Tauqueer M. et al. [12]).

The available literature reveals a significant gap in the study of GFRP for subsea pipeline protection against dropped object impact. Besides the research from Tauqueer M. et al., most existing peer-reviewed literature focuses on steel structures or concrete coatings, leaving a limited understanding of the impact energy absorption capacity of GFRP protective structures.

While considerable advancements have been made in assessing the impact of dropped objects on subsea pipelines, the need for further research into GFRP protective covers remains evident. This study aims to address this gap by leveraging NLFEA simulations.

2.3 GFRP molded gratings

GFRP molded gratings are offered as a proven option for protecting subsea equipment. Grid structures offer excellent energy absorption capabilities. The rectangular grid shape closely resembles a cellular structure, making it highly effective for energy absorption. As opposed to conventional gratings, molded GFRP gratings usually don't have a primary load-bearing direction due to the manufacturing process, which often results in similar cross-section properties and bearing bar spacings in both directions [13]. Such high bidirectional stiffness provides effective load redistribution when subjected to concentrated loads, such as impacts from dropped objects. Due to their characteristics, GFRP gratings are currently used in protection covers of subsea equipment, as shown in Figure 4.

Figure 4. Illustration of implementation of FRP gratings for subsea equipment protection (Obtained from PJNC Ltd UK [14]).

GFRP molded gratings consist of bearing bars, each incorporating glass fiber rovings layered between each lamina. These layers alternate between reinforced and unreinforced laminae per bearing bar or rib [13]. This allows the orthogonal intersecting ribs to fill the cross-section with reinforced lamina to combine strength and bending stiffness in these areas, as illustrated in Figure 5.

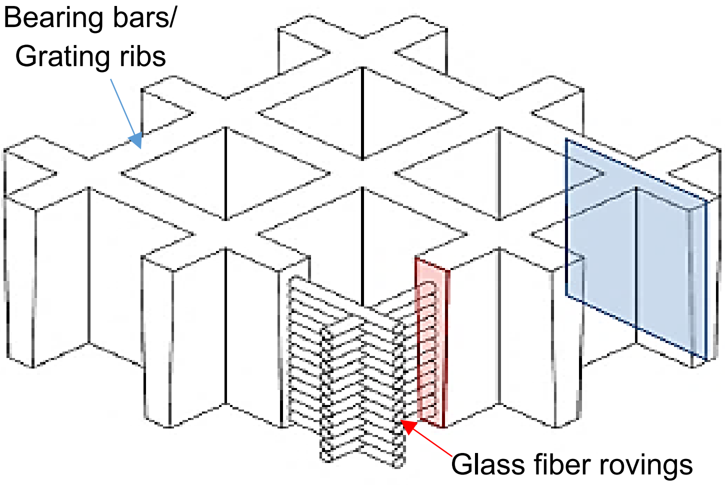

Figure 5. The general structure of a GFRP molded grating (Reproduced from Gattesco et al. [15]).

Various authors have assessed the structural capacity of GFRP molded gratings through numerical and experimental testing. This includes work by Gattesco et al. [15] and from Bien et al. [13]. Although these studies focused on the damage assessment of GFRP molded gratings under quasi-static loading conditions, they were highly valuable for calibrating and validating the material models used in this thesis.

2.4 Applicable standards

The design and analysis of subsea protective equipment must adhere to industry standards to ensure structural integrity and operational safety against impact loads. The primarily applicable codes for subsea pipeline cover design are DNVGL-RP-C204 and DNVGL-RP-F107. These codes provide a robust framework for the design, analysis, and risk management of subsea covers, ensuring they can effectively protect critical subsea equipment from impact loads.

2.4.1 DNVGL -RP-C204

DNV RP-C204 section 4 provides considerations and design principles for dealing with dropped object impact. The impacting load is characterized by the kinetic energy of the dropped object [16]. The effective kinetic or impact energy is calculated using the following equation:

$$E_{kin} = \frac{1}{2}(m + a){v_t}^2 \tag{2.1}$$

Where,

E_{kin} is the kinetic energy of the dropped object.

a is the hydrodynamic added mass.

m is the mass of the object.

v_t is the terminal velocity.

To calculate the total kinetic energy of the object before impacting the subsea equipment, the terminal velocity term is introduced into equation 2.1. The terminal velocity considers the effects of the drag force and buoyancy force balance, which is calculated using the following equation:

$$v_t = \sqrt{\frac{2g(m - \rho_w V)}{\rho_w C_d A_p}} \tag{2.2}$$

Where,

ρ_w is the density of seawater.

A_p is the projected cross-sectional area of the object.

C_d is the drag coefficient.

V is the object displacement.

g is gravity.

The kinetic energy from the object is absorbed in the form of strain energy by the impacted structure [16]. The energy balance dictates how much energy is left after the object has penetrated the equipment, if any. This relationship is illustrated in Figure 6.

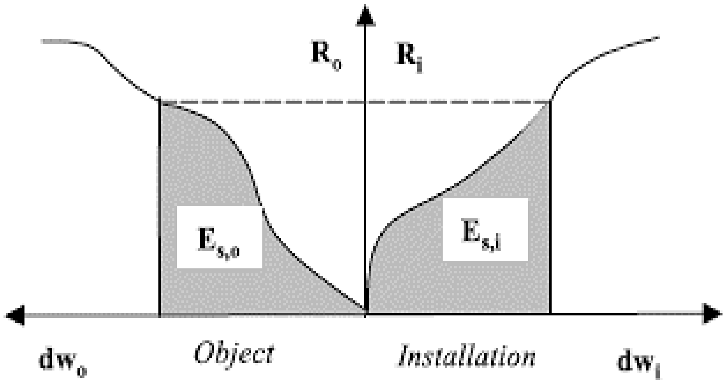

Figure 6. Absorption of dropped object kinetic energy as strain energy in the installation (Obtained from DNV RP-C204 [16]).

2.4.2 DNVGL RP-F-107

DNV RP-F-107 focuses on the pipeline protection capacity after accidental loading scenarios that can damage the pipeline due to the impacting loads from dropping objects. This recommended practice states that the total energy absorbed by the pipeline and indenting object penetration are used to assess the total damage of the pipeline after the impact.

The equation below is proposed to assess the maximum energy the pipeline can absorb before it sustains significant damage and leakage, considering a knife-edge load perpendicular to the pipeline [5]. The equation gives a conservative estimate of the pipeline energy absorption capacity, as it does not consider the effects of soil conditions and pipeline coating.

$$E_{abs} = 16 \cdot \left(\frac{2\pi}{9}\right)^{\frac{1}{2}} \cdot m_p \cdot \left(\frac{D}{t}\right)^{\frac{1}{2}} \cdot D \cdot \left(\frac{\delta}{D}\right)^{\frac{3}{2}} \tag{2.3}$$

Where,

δ is the pipeline deformation or dent depth.

D is the pipe outer diameter.

$\mathrm{E_{abs}}$ is the energy absorbed.

m_p is the plastic moment capacity of the wall.

t is the pipe thickness.

As per section 4 of this recommended practice, any dent penetration higher than 5% of the diameter could lead to potential leakage and major damage to the pipeline. Thus, according to equation 2.3, for the subsea 20-inch pipe with a 0.5-inch wall thickness referenced in this study, the maximum kinetic energy of the dropped object should not exceed 6.87 kJ to prevent potential leakage. Although this work does not study the impact of a dropped object on the pipeline, it is important to understand the underlying variables affecting pipeline damage.

Since the amount of protection required to avoid damage to pipelines varies according to pipe diameter, dent size, and kinetic energy of the dropped object, this recommended practice states that protective tunnel structures should typically have an impact resistance of at least 50 kJ [5].

3 Methodology

3.1 FEM for analysis of non-linear dynamic systems

The Finite Element Method (FEM) is a versatile computational tool that can be used to solve field problems for which it is difficult to obtain analytical solutions, providing a spatial representation of one or more dependent field variables, e. g stress, displacement, and temperature. FEM is a method based on dividing or discretizing the domain into small elements which are connected by nodes. The discretized governing equations are then solved along the partitioning of the domain in a piecewise fashion to give an approximate solution of the field quantities over the entire domain [17].

The basic assumption of structural analysis in FEA lies in the linear relationship between stress and strain, which remains valid as long as the deformation caused in the structure does not go beyond the elastic range. This means the structure can return to its previous form after removing the load. However, when the load-structure interaction induces plastic deformation, the relationship becomes non-linear, and a non-linear equilibrium path governs the structural response [18]. This introduces physical non-linearities to the system, significantly complicating the analysis.

Non-linear effects in a system can arise from many causes, the most common of which are material non-linearities, geometric non-linearities, and boundary condition non-linearities (contacts). These non-linearities are present in systems subjected to dynamic impact loads, making the structural response calculations quite complicated. Analyzing such systems requires the use of non-linear finite element solvers. Therefore, advanced FEA algorithms and robust material models are required to accurately capture the complex interactions within the structure.

On the other hand, appropriate modeling of the dynamic system is key for studying dropped object impact. The dynamic equation of motion defines the Initial Value Problem (IVP) of a dynamic system:

$$\begin{cases} M\ddot{u}(t) + C\dot{u}(t) + Ku(t) = f(t) \\ u(t_0) = u_0, \dot{u}(t_0) = \dot{u}_0 \end{cases} \tag{3.1}$$

Where,

M is the mass matrix.

K is the stiffness matrix.

u are the displacements.

$\dot{\mathrm{u}}$ are the velocities.

$\ddot{\mathrm{u}}$ are the accelerations.

f is the external force vector.

The general equation is solved for each discretized element at discrete points in time. The IVP can be discretized to account for the time step so that the equilibrium equations are satisfied at discrete time intervals [19]. The discretized equation changes to:

$$\begin{cases} M\ddot{u}_{k+1} + C\dot{u}_{k+1} + Ku_{k+1} = f(t_{k+1}) \\ u(t_0) = u_0, \dot{u}(t_0) = \dot{u}_0 \end{cases} \tag{3.2}$$

Where,

$\ddot{u}_{k+1}$, $\dot{u}_{k+1}$, u_{k+1}, are the acceleration a, velocity, and displacement vectors at time t_{k+1}.

There are two methods for integrating the IVP: implicit and explicit. The accuracy of both methods depends on the chosen time step and the assumptions made when discretizing the domain and applying the boundary conditions [19]. Since dropping object simulations in this study were performed using the explicit solver, the following subsections provide further details about its fundamental principles.

3.1.1 Explicit solvers

Explicit solvers are a robust option for dynamic analyses, as the solution scheme does not require matrix inversion or iterations and, therefore, is more computationally effective than implicit solvers [20]. However, explicit methods employ variables from the previous time instant, which means they are conditionally stable based on the critical time step chosen. The critical time-step size is governed by the Courant-Friedrichs-Lewis (CFL) condition and depends on the element type, size, and material properties. The critical timestep is defined by the following equation:

$$\Delta t_e = \frac{L_e}{[Q + (Q^2 + c^2)^{1/2}]} \tag{3.3}$$

Where,

Δt_e is the critical time step size for solid elements.

Q is a function of the bulk viscosity.

c is the adiabatic sound speed of the material, which for elastic materials is defined as:

$$c = \sqrt{\frac{E(1-\upsilon)}{(1+\upsilon)(1-2\upsilon)\rho}} \tag{3.4}$$

Where,

ρ is the material density.

υ is the Poisson ratio.

E is the Young's modulus of the material.

The critical time step is essential to avoid contact instabilities. Due to the small time step magnitude and a relatively large number of time steps before the predefined end time of the analysis is reached, the use of solvers with double precision is imperative [20].

3.2 Tools

Several computational tools were used to assess the highly non-linear and complex behavior of GFRP gratings following the impact of the dropped object.

3.2.1 LS-DYNA

LS-DYNA was the software used to perform all the FEA simulations presented in this study. LS-DYNA is a finite element code designed for analyzing highly non-linear problems, including large deformation structural static analyses and the non-linear dynamic response of structures, including Lagrangian fluid interaction [21]. The central solution methodology is based on explicit time integration. The software includes several material and contact formulations, providing the flexibility to model the structural interaction of various physical systems.

3.2.2 High-Performance Computing (HPC)

Obtaining solutions for the discretized structures requires solving the motion equations and the contacts for each element. This solution process consumes considerable computational resources as the complexity of the models and the interactions of variables increase when introducing non-linear terms. Therefore, parallel computing using a High-Performance Cluster comes in handy to reduce the computation time.

HPC systems aggregate multiple processors and memory modules through ultra-high-bandwidth interconnections to enable parallel processing. The computational power of computers is measured in units called "FLOPS" (floating point operations per second). "FLOPS" describes a theoretical processing speed; achieving this speed requires continuously delivering data to the processors [22].

The HPC used for this research is the Fram, located at the Arctic University of Norway, and named after the Norwegian Arctic expedition ship Fram. This research supercomputer is capable of 1.1 Petaflops per second at theoretical peak performance [23], which is about 1 million times the computing power of a high-end personal computer.

3.2.3 MATLAB

MATLAB is a powerful, well-known software package used in many engineering and scientific applications for data analysis, simulations, and modeling of complex systems. It has built-in optimization functions and features some data analytics for linear and highly nonlinear models. MATLAB offers robust algorithms for non-linear regression optimization problems, such as Kriging and the Multi-Objective Genetic Algorithm (MOGA), used to model the response surface and optimize the GFRP grating dimensions respectively.

3.3 Geometries

The geometry of both the dropped object and the protective cover was created and discretized in LS-DYNA. The geometric details of both objects are discussed in the following subsections.

3.3.1 Dropped object

The dropped object is a tank of S355 steel. The original dimensions of the tank are detailed in Table 1 and Figure 7. All the connections between the tank and the frame members are assumed to be bonded.

Table 1. Sections of the tank and frame.

Section	Description
1	SHS 80mm. t=8mm
2	RHS 20x10mm. t=6mm
3	SHS 80mm. t=5 mm
4	SHS 150mm. t=15mm
5	Saddle supports. t=10mm
6	Reinforcement plate 400x420mm
7	RHS 10x5mm. t=6mm
8	RHS 300x150mm. t=6mm
9	Tank shell 1600mm diameter. t=4mm
10	Tank shell reinforcements. t=10mm
11	Tank head. t=5mm

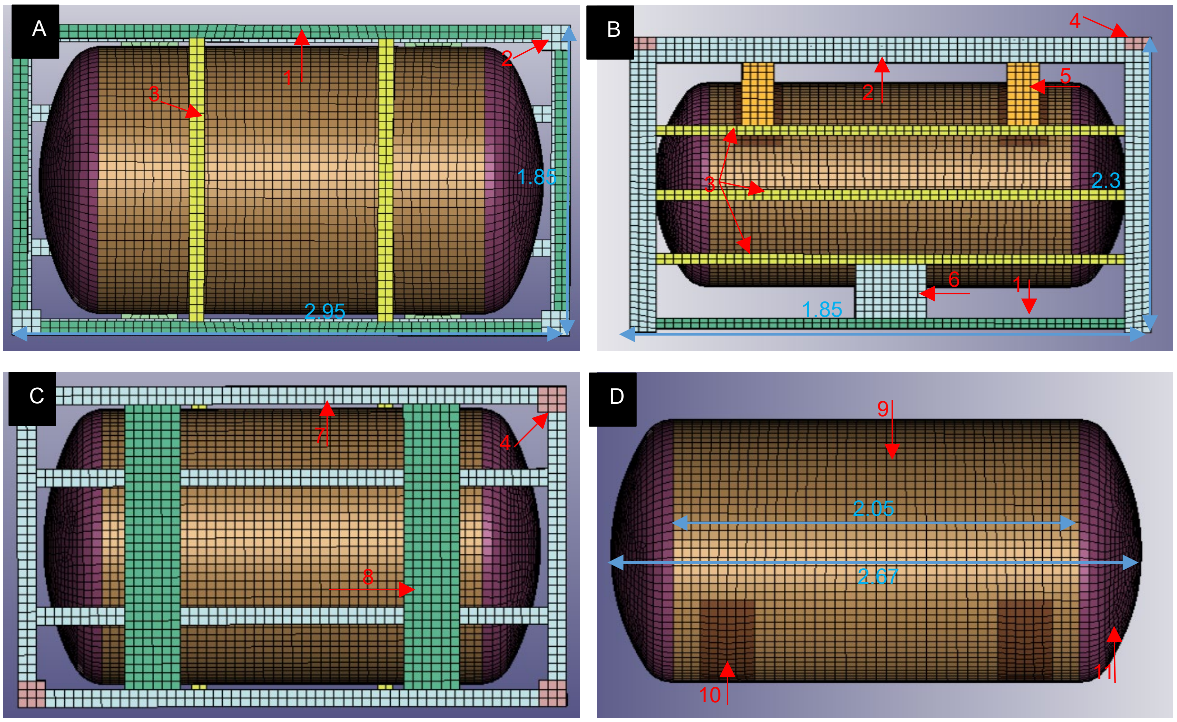

Figure 7. Dimensions of the tank frame from: top view (A), front view (B), side view (C), and only tank front view (D). All dimensions are in meters.

3.3.2 Protective cover

Due to limitations in computational resources, simulating the interaction of the entire cover structure was prohibitive. Therefore, this study focused on assessing the energy absorption capacity of the GFRP molded gratings placed on top of the proposed tunnel protective structure. However, the conceptual geometry of the protective cover had to be defined as it sets the boundary conditions for the simulation models.

The cover was dimensioned based on a 20-inch pipe with a 0.5-inch wall thickness, adapted from the proposed geometries by Tauqueer et al. [12], assuming these were based on real dimensions of structures used in subsea pipeline protection. The proposed cover concept, shown in Figure 8, is a trapezoidal-shaped tunnel structure. The cover is assumed to be properly constrained, meaning it does not suffer large deformations or buckling during impact

The dimensions of the GFRP gratings will be varied to determine the optimal size for maximum energy absorption at the lowest possible cost (see section 5.3). To simplify the geometry of the grating for the FEA model, the grating ribs were modeled with rectangular cross-sections instead of the typical trapezoidal shape found in molded gratings to facilitate unmolding [13]. The ribs of GFRP molded gratings are composed of alternating reinforced and unreinforced laminae in the longitudinal and transversal directions.

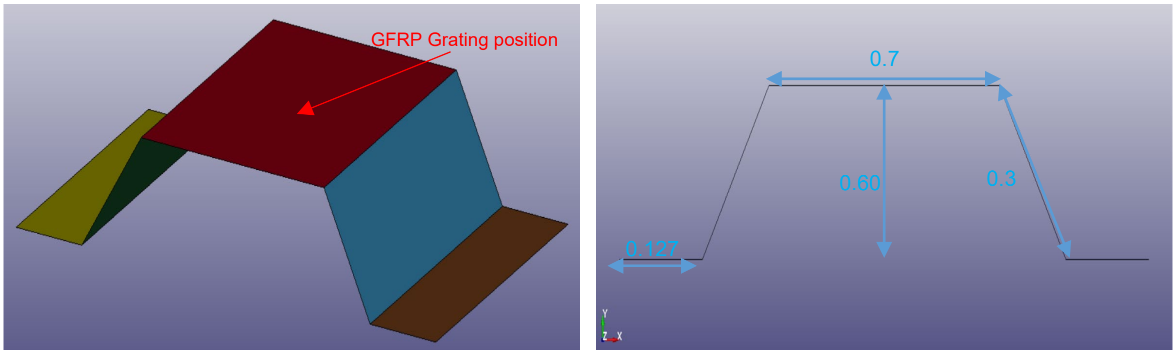

Figure 8. Conceptual design of the tunnel structure: Isometric view (left) and front view (right). All dimensions are in meters.

The effects of the following geometric parameters on the energy absorption capacity of the gratings will be studied: rib width (W), grating thickness (H), and grid pitch (P). Since the variations in glass fiber roving size are not assessed in this research, the laminate thickness (t) is fixed at 1.9 mm. Additionally, since the roving size is constant, an increase in rib thickness is assumed to affect the fiber volume content of the grating in this study. The geometric variables of the grating are illustrated in Figure 9.

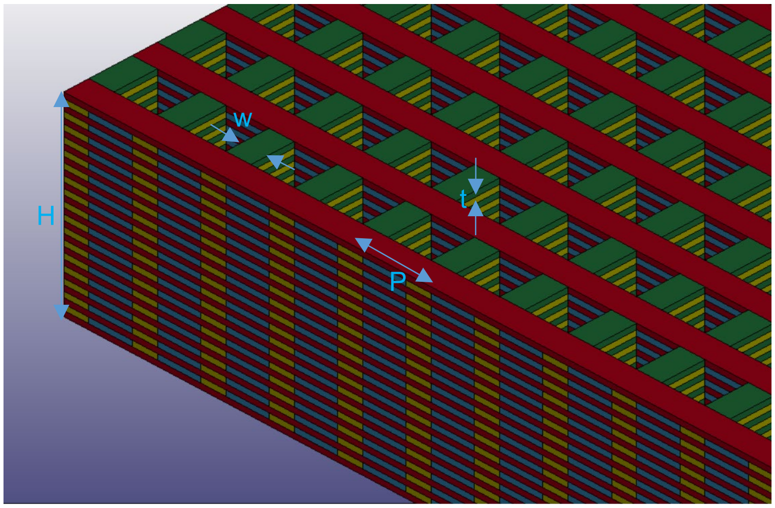

Figure 9. Characteristic dimensions of GFRP molded gratings.

3.4 GFRP mechanical properties

The mechanical properties of the GFRP were obtained from peer-reviewed literature and calibrated based on previous studies on molded GFRP gratings. The base materials for the grating are a thermoset epoxy resin for the matrix and glass fiber type E for the glass fiber roving. The mechanical properties of the base materials used in the composite micromechanics calculations are shown in Table 2.

Table 2. Mechanical properties of base materials of GFRP gratings [13].

Property	Glass fiber	Epoxy resin
Density (g/cm^3)	2.57	1.55
T (tex)	2415	-
Young's modulus (GPa)	70.00	5.75
Poisson ratio	0.220	0.335
Tensile strength (MPa)	2150	72
Compressive strength (MPa)	2150	115
Shear strength (MPa)	-	46

Based on the 3-point bending test performed by Bien et al. [13], the cross-section and inertia of the trapezoidal-shaped rib were calculated to find an equivalent rectangular shape. A rib thickness of 5.9 mm provided similar inertia to the trapezoidal shape studied in their paper. Thus, the fiber volume fraction was assumed to be 30%, as in their study.

Since composite laminates are inherently orthotropic, the mechanical properties of the laminate were calculated using the principles of composite micromechanics, which will be detailed in the following subsections of this document. The mechanical properties of the laminate vary for each plane formed by the laminate ply axes. The laminate ply axes referenced in the strength calculations are indicated in Figure 10.

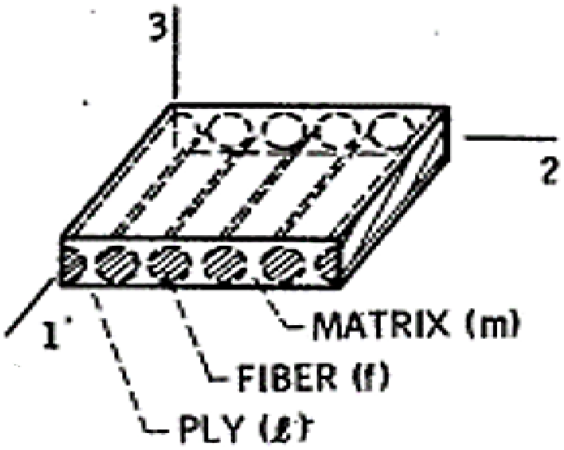

Figure 10. Laminate ply axes (Obtained from Research Lewis Center [24])

To simplify the notation of the variables presented in the following subsections, the following notation is used to denote the mechanical properties of each plane formed by the laminate axes (See Figure 10).

- 1_1 Fiber longitudinal direction
- 1_2: Laminate transverse-longitudinal in-plane direction
- 1_3: Laminate transverse-longitudinal through-thickness direction
- 2_2: Transverse in-plane direction
- 2_3: Laminate transverse-transverse through-thickness direction
- 3_3: Transverse through-thickness direction

3.4.1 Longitudinal mechanical properties

The glass fiber roving exhibits its highest strength properties in the longitudinal direction. The mechanical properties of the laminate are calculated based on the fiber volume fraction using the following set of formulas:

$$E_{l11} = k_f \cdot E_{f,1\_1} + k_m \cdot E_m \qquad 3.5$$

Where,

E_f is the Young's modulus of the fiber.

E_l is the Young's modulus of the laminate.

E_m is the Young's modulus of the resin matrix.

$\mathrm{k_f}$ is the volume fraction of the fiber.

$\mathrm{k_m}$ is the volume fraction of the resin matrix.

The tensile and compressive strength of the laminate are linearly proportional to the fiber volume fraction and its longitudinal strength. This relationship is expressed through the following equations:

$$S_{lT,1\_1} = k_f \cdot S_{fT,1\_1} \qquad 3.6$$

$$S_{lC,1\_1} = k_f \cdot S_{fC,1\_1} \qquad 3.7$$

Where,

S_{fT} is the tensile strength of the fiber.

$\mathrm{S}_{f\mathrm{C}}$ is the compressive strength of the fiber.

$\mathrm{S_{lT}}$ is the tensile strength of the laminate.

$\mathrm{S_{lC}}$ is the compressive strength of the laminate.

3.4.2 Transverse mechanical properties

The calculation of the mechanical properties of the laminate in the transverse direction depends on the ply material axis. The transverse modulus, shear modulus, and Poisson's ratio are calculated using the following formulas:

$$E_{l,2\_2} = \frac{E_m}{1 - \sqrt{k_f} \cdot \left(1 - \frac{E_m}{E_{f,2\_2}}\right)} = E_{l,3\_3} \tag{3.8}$$

$$G_{l,1\_2} = \frac{G_m}{1 - \sqrt{k_f} \cdot \left(1 - \frac{G_m}{G_{f,1\_2}}\right)} = G_{l,1\_3} \tag{3.9}$$

$$G_{l,2\_3} = \frac{G_m}{1 - k_f \cdot \left(1 - \frac{G_m}{G_{f,2\_3}}\right)} \tag{3.10}$$

$$\nu_{l,1\_2} = k_f \cdot \nu_{f,1\_2} + k_m \cdot \nu_m = \nu_{l,1\_3} \tag{3.11}$$

$$\nu_{l,2\_3} = k_f \cdot \nu_{f,2\_3} + k_m \cdot \left(2\nu_m - \nu_{l,1\_2} \cdot \frac{E_{l,2\_2}}{E_{l,1\_1}}\right) \tag{3.12}$$

Where,

ν_f is the Poisson's ratio of the fiber.

ν_l is the Poisson's ratio of the laminate.

ν_m is the Poisson's ratio of the resin matrix.

G_f is the shear modulus of the fiber.

G_l is the shear modulus of the laminate.

G_m is the shear modulus of the resin matrix.

The tensile and compressive transverse strength, as well as the intralaminar shear strength of the laminate, can be calculated using the following formulas:

$$S_{lT,2\_2} = \left[1 - \left(\sqrt{k_f} - k_f\right) \cdot \left(1 - \frac{E_m}{E_{f,2\_2}}\right)\right] \cdot S_{mT} \tag{3.13}$$

$$S_{lC,2\_2} = \left[1 - \left(\sqrt{k_f} - k_f\right) \cdot \left(1 - \frac{E_m}{E_{f,2\_2}}\right)\right] \cdot S_{mC} \tag{3.14}$$

$$S_{lS,1\_2} = \left[1 - \left(\sqrt{k_f} - k_f\right) \cdot \left(1 - \frac{G_m}{G_{f,1\_2}}\right)\right] \cdot S_{mS} \tag{3.15}$$

Where,

S_{lS} is the shear strength of the laminate.

S_{mC} is the compressive strength of the resin matrix.

S_{mT} is the shear strength of the resin matrix.

S_{mT} is the tensile strength of the resin matrix.

3.5 GFRP energy absorption

The energy absorption of composite materials is influenced by several factors, including fiber orientation, laminate stack-up, fiber and matrix material, fiber-matrix interface, volume content, as well as cross-sectional and lengthwise shape [1].

Although the interactions at a macroscopic level between the laminates and the modes of failure of a GFRP structure—such as delamination and debonding—are complex, one can analyze the factors that affect the through-thickness impact resistance (energy absorbed per unit volume) per lamina [24]:

$$\gamma_{lS,2\_3} = \frac{[1-a]^2 \cdot {S_{mS}}^2}{2G_m \cdot \left[1 - k_f \cdot \left(1 - \frac{G_m}{G_{f,2\_3}}\right)\right]} \tag{3.16}$$

$$\gamma_{lF,2\_2} = 4.5 \cdot [1-a]^2 \cdot \left\{\frac{\left[1 - \left(\sqrt{k_f} - k_f\right) \cdot \left(1 - \frac{E_m}{E_{f,2\_2}}\right)\right]}{\left(1 + \frac{S_{mT}}{S_{mC}}\right)}\right\}^2 \cdot c \tag{3.17}$$

Where,

$\gamma_{l\mathrm{F},2\_3}$ is the flexural through thickness impact resistance.

$\gamma_{lS,2\_3}$ is the interlaminar shear through thickness impact resistance.

$$a = \sqrt{k_f} \cdot \left(1 - \frac{\mathrm{E}_m}{\mathrm{E}_{f,2\_2}}\right)$$

$$b = \frac{\mathrm{S}_{mS}^2}{2\mathrm{G_m}}$$

$$c = \frac{\mathrm{S}_{mT}^2}{\mathrm{E_m}}$$

It can be noted that the fiber volume fraction content significantly influences the flexural impact resistance. However, the through-thickness shear impact resistance decreases as the fiber volume content increases. Since the impacting object exerts through-thickness penetration, it is expected that the geometric dimensions of the grating will have a greater influence on the structural behavior of the grating than the total fiber volume fraction.

3.6 Material damage models

Both the protective cover and the impacting object will undergo large plastic deformation during the impact, which will lead to large deformations and damage. Hence, it is important to use an appropriate material failure criteria in the FEM code to account for this. LS-DYNA offers several damage formulations to accurately represent the physical behavior of the impacting bodies. The material models used in this research will be discussed in the following subsections.

3.6.1 MAT054

GFRP molded gratings can have different failure mechanisms that induce brittle failure or progressive degradation of the multilayer composite [13]. Local micro-scale phenomena, such as local fiber-matrix debonding and delamination, are also failure modes that must be modeled accurately to study laminate failure.

The MAT_ENHANCED_COMPOSITE_DAMAGE (MAT054) material card in LS-DYNA was selected to model the GFRP components since it accounts for the nonlinear shear stress-strain behavior, fiber failure modes, and post-stress degradation [25]. This material model implements the use of the Chang-Chang criterion for matrix failure. The compressive failure mode of the matrix and the fiber are defined from the equations 3.18 and 3.19 respectively, whereas the tensile failure mode of the matrix and the fiber are defined from equations 3.20 and 3.21 respectively.

$$0 \leq \left(\frac{\sigma_{1\_1}}{S_{lT,1\_1}}\right)^2 + \beta\left(\frac{\sigma_{1\_2}}{S_{lS,1\_2}}\right)^2 - 1 \tag{3.18}$$

$$0 \leq \left(\frac{\sigma_{1\_1}}{S_{lC,1\_1}}\right)^2 - 1 \tag{3.19}$$

$$0 \leq \left(\frac{\sigma_{2\_2}}{S_{lT,2\_2}}\right)^2 + \beta\left(\frac{\sigma_{1\_2}}{S_{lS,1\_2}}\right)^2 - 1 \tag{3.20}$$

$$0 \leq \left(\frac{\sigma_{2\_2}}{2S_{lS,1\_3}}\right)^2 + \left[\left(\frac{S_{lC,2\_2}}{2S_{lS,1\_3}}\right)^2 - 1\right] \cdot \frac{\sigma_{2\_2}}{S_{lC,2\_2}} + \left(\frac{\sigma_{1\_2}}{S_{lS,1\_2}}\right)^2 - 1 \tag{3.21}$$

Where,

σ_{1_1} is the longitudinal stress.

σ_{1_2} is the transverse-longitudinal in-plane stress.

σ_{1_2} is the intralaminar shear stress.

σ_{2_2} is the transverse in-plane stress.

Failure in the composite laminate can occur through several mechanisms, which are determined by specific parameters specified in the material card in LS-DYNA. For the GFRP molded gratings studied in this paper, failure occurs when the fiber strain exceeds the maximum tensile fiber strain in tension (7.8% [26]) or the maximum tensile fiber strain in compression (4.0% [27]). The parameters specified in the material card for the reinforced and unreinforced laminae of the GFRP gratings are found in Appendix A.2 and Appendix A.3.

LS-DYNA deletes the affected elements after the failure of the layers across the through-thickness integration points. This deletion creates what is referred to as "crashfront" elements [21]. These elements, which share nodes with the deleted element, may experience a reduction in strength.

Note that some of the notations in the above-presented formulas have been adapted for this paper. For the original notation and further explanation of the parameters used in the material card, refer to the LS-DYNA Theory Manual [21].

3.6.2 MAT024

The MAT_PIECEWISE_LINEAR_PLASTICITY material card models the elastoplastic behavior of the material as a function of strain at a given strain rate. The Cowper-Symonds equation is used to model perfectly plastic behavior with dynamic sensitivity to the strain rate [8]. The dynamic stress can be calculated by introducing the Cowper-Symonds model parameters:

$$\sigma_d = \sigma_0 \left[1 + \left(\frac{\dot{\varepsilon}}{C} \right)^{1/p} \right] \qquad 3.22$$

Where,

σ_0 is the static yield strength.

σ_d is the dynamic yield strength.

$\dot{\varepsilon}$ is the strain rate.

C and p are material parameters.

For S355, the experimental values for the model parameters at a strain rate of $40 s^{-1}$ are C=40 and p=5. It is important to be cautious when using these values since the strain rate can vary during impact. Therefore, material parameters should be calculated based on an average strain rate [8]. For further explanation on the calculation of material hardening and deviatoric stress, refer to the LS-DYNA theory manual [21]. The stress-strain curve used for the dropping object can be found in section 4.3.1 of this paper. The material card for the deformable tank model is given in Appendix A.4.

3.7 FEA Numerical modeling

The accuracy and reliability of FEA results are governed by several factors, including model geometry, discretization, and boundary conditions. Each of these elements plays an important role in the simulation outcome. A general schematic of the interaction between these variables in the LS-DYNA model used in this research is shown in Figure 11. Also, Appendix A. 1 shows a flowchart illustrating the methodology followed for the analysis performed in this research.

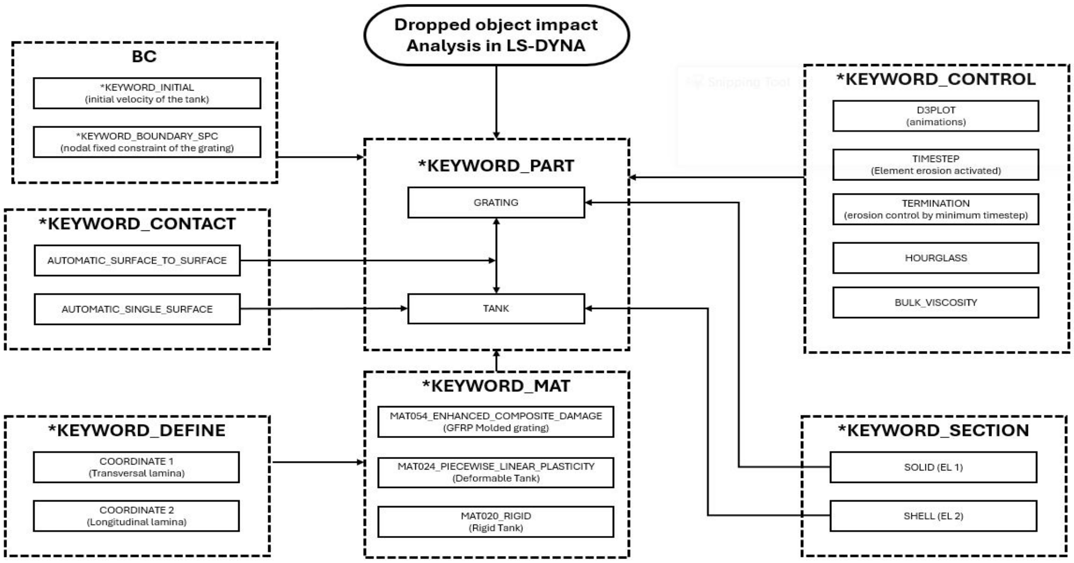

Figure 11. Flowchart for NLFEA simulation of dropped object impact in LS-DYNA.

3.7.1 Contact formulations and element type

The proper definition of contacts between the impacting bodies is essential for correctly representing the impact physics. Contacts can be defined in LS-DYNA between parts, nodes, and part sets.

In this study, the contact between the dropping object and the GFRP components was defined using the keyword card CONTACT_AUTOMATIC_SURFACE_TO_SURFACE. Setting the details of the interaction between the slave and master nodes or surfaces of the bodies in contact is crucial to prevent inaccuracies in the simulation. In explicit analysis, the moving or less stiff object is designated as the slave, while the fixed or stiffer object is defined as the master.

The GFRP grating was modeled using under-integrated constant-stress solid elements (element formulation EL 1 in LS-DYNA) for the dropped object impact simulations. The constant stress solid element can sustain large deformations and is the most effective element type for impact analysis [28]. However, this element is susceptible to hourglass modes, and hourglass control needs to be applied to avoid spurious behavior.

For the quasi-static 3-point bending test, fully integrated quadratic elements with 8 nodal rotations (element formulation EL 3 in LS-DYNA) were used. On the other hand, the deformable sections of the tank were modeled using under-integrated Belytschko-Tsay shell elements with five through-thickness integration points. Refer to the LS-DYNA documentation for more details about the element and contact formulations [29].

3.7.2 Boundary conditions

As mentioned before, due to computational constraints, the structural behavior of the whole protective cover proposed in section 3.3.2 is not modeled in this study and is assumed to be properly constrained. This means the cover will not buckle or deform excessively during the impact. Therefore, the simulation domain consisted of the GFRP grating with its boundaries constrained in all directions for both displacements and rotations, and the tank with initial velocity.

Since the boundaries in the transverse direction of the grating depend on the proposed tunnel structure width (0.7 m), the dropped object had to be scaled down in all directions by a factor of 8 (see section 4.3.1).

The initial velocity of the dropped object before impact was calculated using equation 2.2. Since the rotation of the dropping object and its influence on energy absorption are challenging to quantify precisely [8], only an initial vertical velocity (perpendicular to the grating surface) was applied to the tank. The boundary conditions and physical properties of the tank are summarized in Table 3. Since the inertial forces dominate the structure's response during the impact, the simulations did not account for the hydrodynamic effects.

Table 3. Boundary conditions.

mass (kg)	6451.8
Initial velocity (m/s)	5.5
Drag coefficient Cd	0.7 [6]
Kinetic energy (kJ)	99.1

3.8 Structural optimization

The cost of GFRP molded gratings depends significantly on the total material (weight), the number of glass fiber rovings, and the fiber volume content. Therefore, an optimization algorithm that explores the design space to identify the geometry that offers the best balance between absorbed energy and cost is needed to avoid a suboptimal design. The following subsections briefly describe the models used to optimize the grating geometry.

3.8.1 Design of Experiments (DoE) and Response Surface Methodology (RSM)

Due to the highly non-linear interactions of the studied geometric parameters of the GFRP gratings, analytical methods alone cannot accurately predict their influence on the total energy absorbed from impact. Therefore, it was necessary to design experiments to statistically quantify their influence.

Due to computational constraints, the size of the full-factorial design was cost-prohibitive. Hence, an experimental screening was executed using a Central Composite Design (CCD) since it can manage the interaction of the three independent geometric variables of the GFRP grating with a good degree of repeatability for robust modeling.

On the other hand, the Response Surface Methodology (RSM) encompasses a set of mathematical methodologies employed to construct an empirical model from the statistically designed experiments. RSM leverages multiple polynomial regression equations to capture functional relationships between the geometric variables of the grating and the response values. Through regression analysis, RSM optimizes process parameters and predicts the response values, contributing to a more comprehensive understanding of the trade-off between variables and desired outcomes [30].

Hence, the response surface function is derived from the Design of Experiments (DoE), offering approximations of output parameters across the design space without needing a complete solution. Different types of response surface models, ranging in complexity and accuracy, are available. Since the number of interacting variables is relatively small and the problem is highly non-linear, the Kriging method was selected to study the system's response.

Kriging is a Gaussian process Regression model used when dealing with highly non-linear data to generate a prediction model for the response surface [31], Kriging is used to create a smooth, predictive surface from a limited number of expensive evaluations of the actual system, such as in physical experiments or complex simulations. The benefit of this model is that it equals the optimal prediction for a large Gaussian model and generates an unbiased and minimum prediction variance [32].

The heart of the Kriging model is the kernel or covariance function. This function defines the expected covariance between any two points in the input space based on their relative locations or distances. Since this work is not focused on studying the Kriging model structure and its working principle, further explanations of the covariance functions and hyperparameters won't be addressed but can be found in the referenced literature.

3.8.2 Genetic Algorithm (GA) optimization

Structural optimization can be categorized into shape, topological, and sizing optimization [33]. This study focuses on sizing optimization to generate the best geometries with the highest energy absorption capacities per material cost. There is a trade-off between maximizing energy absorption and minimizing the total weight and volume fraction of the GFRP grating. Hence, the Multi-Objective Optimization Genetic Algorithm (MOGA) was chosen to handle this optimization problem. To this end, the MATLAB built-in algorithm for MOGA in the data analysis and optimization toolset was used.

The Genetic Algorithm (GA) is an optimization strategy based on the theory of natural selection. The model is inspired by biological systems, where populations of organisms (generated data points) evolve over many generations to fit the fitness functions best [33]. The genetic algorithm performs optimization through the evolution of a population of organisms (data points). Each organism represents a possible optimal solution to the optimization problem and competes to find the best solution. The fittest organisms mate to generate a new population of subjects, which undergo random mutations to replace the parents. This process is iterated until, through many generations, the quality of artificial organisms improves, resulting in optimization.

Design variables are the chromosomes in the context of the genetic algorithm. The chromosomes are usually a one-dimensional gene string in which the value assigned to each location is 0 or 1. Since chromosomes must each define the design variables in the optimization, they are divided into parameters, with the number of parameters in each chromosome equaling the number of design variables for the optimization.

Since the primary focus of this thesis is not to delve into the Genetic Algorithm, the process and formulas for generating organisms after each mutation will not be described in detail. For further study of the generated population, one can refer to Chapman's work [33].

Based on the author's observations from FEA simulation results, penalties were introduced for candidates with a volume fraction outside the 20% to 40% range and for gratings exceeding 60 kg/m to avoid biasing the MOGA optimization.

4 Model validation

4.1 Material model verification

Since various parameters affect the damage and failure of the composite, the material model had to be calibrated based on results from 3-point bending experimental tests. The mechanical properties of the grating were explicitly compared against the quasi-static 3-point bending test performed by Bien et al. [13]. The 3-point bending test FEA model is shown in Figure 12, and the relevant values of the test setup are tabulated in Table 4.

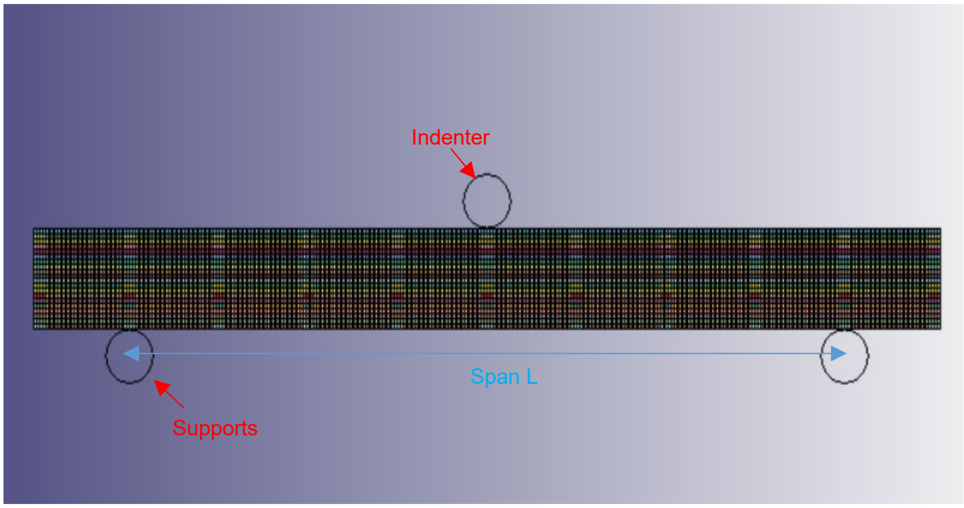

Figure 12. FEA model of 3-point bending test.

Table 4. 3-point bending test setup.

Test load rate (kN/s)	0.5
Displacement rate (mm/s)	0.1
Span between supports L (mm)	152
Grating thickness H (mm)	38.0
Laminate thickness t (mm)	1.9
Rib thickness W* (mm)	5.5
Grid pitch P (mm)	38.1
Fiber volume fraction (Vf)	30%
No. of elements	147840

Due to limitations in computational resources, only the bending failure mode from a span between supports of 152 mm (4H) was studied. The Young's Modulus of the grating can be derived from the load-displacement curve in combination with the following equation [15]:

$$E = \frac{F \cdot L^3}{48 \cdot u \cdot I_{yy}} \qquad 4.1$$

Where,

E is the Young's modulus of the grating.

F is the applied load.

$\mathrm{I_{yy}}$ is the second moment of the area of the ribs.

L is the span length.

u is the displacement of the indenter.

The deviation of the estimated mechanical properties is tabulated in Table 5. As can be observed in Figure 13, the material model used in this study did not exactly replicate the mechanical properties obtained by Bien et al. This discrepancy can be attributed to various factors, including the geometric simplification of the grating ribs' cross-section and using different criteria to model composite failure LS-DYNA (Hashin vs. Chang & Chang for solid elements). The simulations performed to calibrate the material model were computationally expensive, so the current level of deviation was deemed acceptable for this study.

Table 5. Comparison of quasi-static bending numerical simulations.

-	Current study	Bien et al.	% deviation
Young's modulus of the grating (MPa)	23.4	24.7	5.5%
Peak force (kN)	19.8	21	5.9%
Peak stress (MPa)	208	221	5.9%

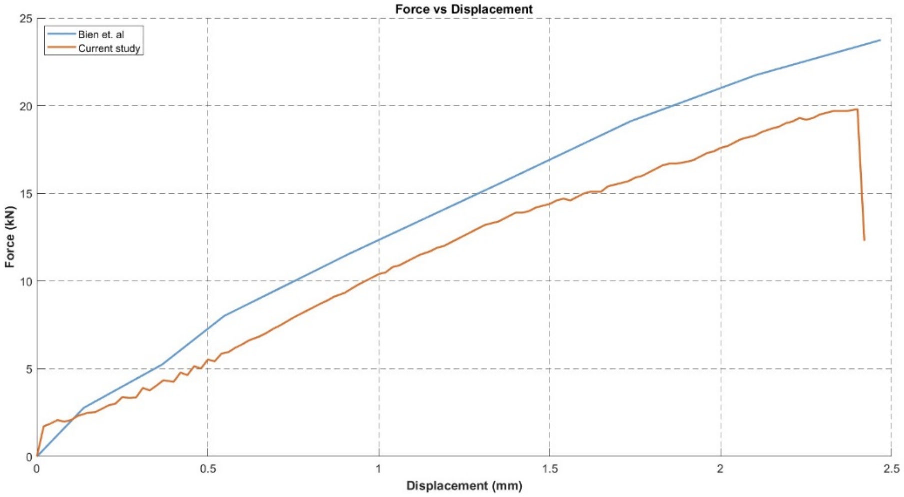

Figure 13. Force vs displacement curves for each study.

4.2 Discussion on convergence

One of the most important steps in FEA is to validate the results obtained from the simulations. In the absence of experimental data for comparison, refining the mesh can help minimize the influence of the discretization method on the results and reduce uncertainty. The following subsections discuss key aspects of numerical convergence in FEA models and the implications of computational resource limitations and computing time.

4.2.1 Mesh

The grating was meshed using a structured mesh composed of quadratic solid elements, with the smallest element size determined by the 1.9 mm thickness of the grating laminae. On the other hand, the tank was meshed using a hybrid unstructured mesh composed of under-integrated shell elements with a minimum element size of 2 mm. The mesh of both bodies is shown in Figure 14.

A mesh sensitivity study was not performed on the dropping object and the grating due to computational limitations. The scaled tank mesh size establishes a critical time step in the order of 1e-7, which is quite small for explicit dynamic simulations. Having elements with a critical time step lower than 1e-7 seconds is excessively costly, requiring a trade-off between computational resources and precision [7].

Ideally, a mesh sensitivity analysis on the grating should have been performed. However, this was prohibitive given the small element size dictated by the thickness of the laminae, falling below 1e-7 for finer meshes. Hence, conducting a sensitivity analysis was deemed unfeasible, given the complexity of the model and the constraints in computational resources. Nonetheless, the author suggests conducting this analysis using a less complex model or more computational resources in future studies.

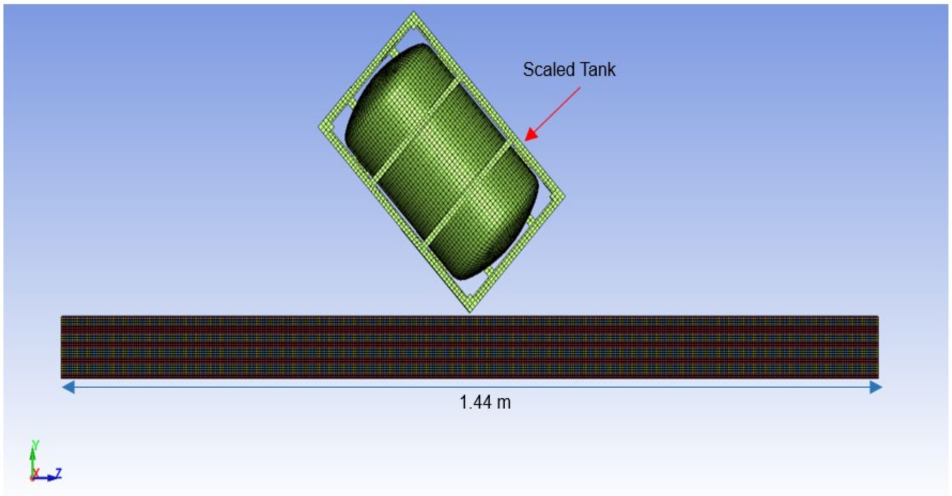

Figure 14. Adjusted domain after tank scaling.

4.2.2 Energy balance

Assessing the energy balance is crucial to determine whether artificial energy is introduced or absorbed due to numerical instabilities, ill-defined contacts, or omitting the hourglass energy from the total energy calculation [28]. The total energy computed by LS-DYNA is calculated using the following equation:

$$U_{total} = U_{kin} + U_{int} + U_{si} + U_{rw} + U_{damp} + U_{hg} \qquad 4.2$$

Where,

$\mathrm{U_{total}}$ is the total energy.

$\mathrm{U_{kin}}$ is the kinetic energy.

$\mathrm{U_{si}}$ is the sliding interface energy.

$\mathrm{U_{rw}}$ is the rigid wall energy.

$\mathrm{U_{damp}}$ is the damping energy.

$\mathrm{U_{hg}}$ is the hourglass energy.

In this study, neither damping nor rigid walls were modeled. Thus, the equation for calculating the total energy for the simulations becomes:

$$U_{total} = U_{kin} + U_{int} + U_{si} + U_{hg} \qquad 4.3$$

The total energy should equal the initial kinetic energy of the dropping object since no initial potential energy or external work is being introduced to the system.

4.2.3 Hourglass

The issue with using under-integrated elements is that zero energy modes arise, known as hourglass modes [21]. Hourglass energy is a numerical issue associated with under-integrated elements and has no meaning in the actual physical behavior of the structure. In other words, it represents artificial deformation not associated with the actual strain energy (See Figure 15).

There are no fixed rules on controlling or reducing the influence of hourglassing. However, it is recommended that the hourglass energy should not be higher than 5% of the total energy of the body of interest [28]. By defining hourglass controls in LS-DYNA, it is possible to add small elastic stiffness in the form of forces capable of stopping the formation of anomalous modes without significantly affecting the stable global modes [21].

Additionally, hourglass energy can be decreased by refining the mesh or using fully integrated elements, which tend to be computationally expensive. Since the velocity of the dropping object in this study was relatively low, an hourglass control of stiffness form was used to reduce the hourglass energy.

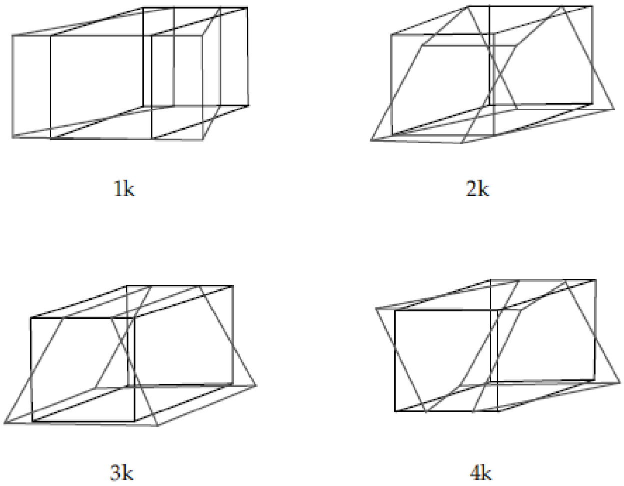

Figure 15. 4 out of 12 total hourglass modes of an eight-node cubic element (Obtained from LS-DYNA theory manual [21]).

4.3 Boundary conditions

It is required that the domain is sufficiently large so that it does not influence the results on the impacted zone [34]. However, due to the imposed size of the cover proposed in section 3.3.2, the width of the GFRP grating is constrained, and the transverse boundaries will influence the plastic stress flow after impact. In contrast, the boundaries in the longitudinal direction could be adjusted to be sufficiently long to avoid interaction during impact.

Due to the high kinetic energy of the tank, avoiding any interaction with the boundaries required extending the longitudinal boundaries to a length that would have been excessively costly in terms of computational resources. After conducting a sensitivity analysis, it was determined that a grating length of approximately 1.44 meters was sufficient to prevent excessive interaction with the longitudinal boundaries during tank penetration, as shown in Figure 16.

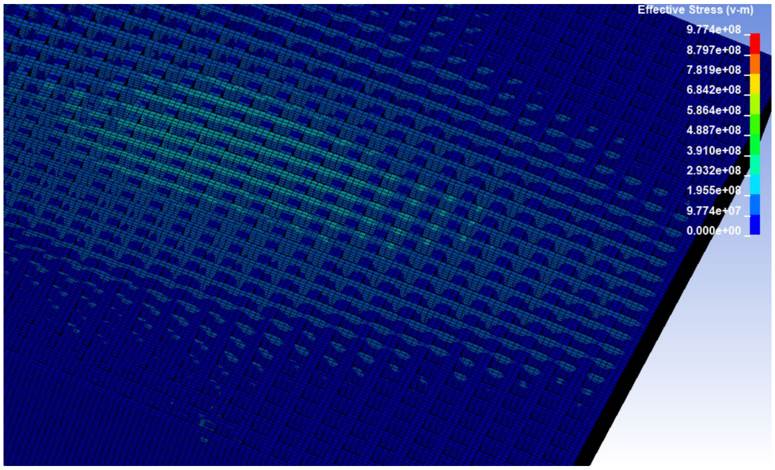

Figure 16. Stress distribution near the extended longitudinal boundaries.

4.3.1 Tank scaling

It is important to note that the tank dimensions were scaled to avoid interaction with the transverse boundaries. Due to the geometric scaling, the absorbed energy per unit area will probably not be the same as the original tank. However, the stiffness of the tank can be replicated to some extent by artificially increasing the strain rate, and thus, the dynamic yield [35].

The mass of the scaled object was artificially increased to replicate the total kinetic energy of the original tank. The scaling laws for structural impact dictate that the dynamic yield of the scaled object changes according to the following formulas [35]:

$$\beta = \frac{L_s}{L_m} \qquad 4.4$$

$$\beta_v = \beta^{q/(q-2)} \qquad 4.5$$

$$\beta_{\sigma d} = \left(\frac{\beta_v}{\beta}\right)^q \qquad 4.6$$

$$\sigma_{ds} = \sigma_d \cdot \beta_{\sigma d} \qquad 4.7$$

Where,

β is the geometric scale factor.

β_v is the impact velocity factor.

$\beta_{\sigma d}$ is the dynamic yield factor.

σ_{ds} is the adjusted dynamic yield for the scaled model.

L_s is the dimension of the smallest or scaled model.

L_m is the actual dimension of the model.

q is $1/p$ being p the material parameter from the Cowper-Symonds model.

Consequently, the stress-strain curve of the S355 is also modified. The stress-strain curves of both the original tank and the scaled model are shown in Figure 17.

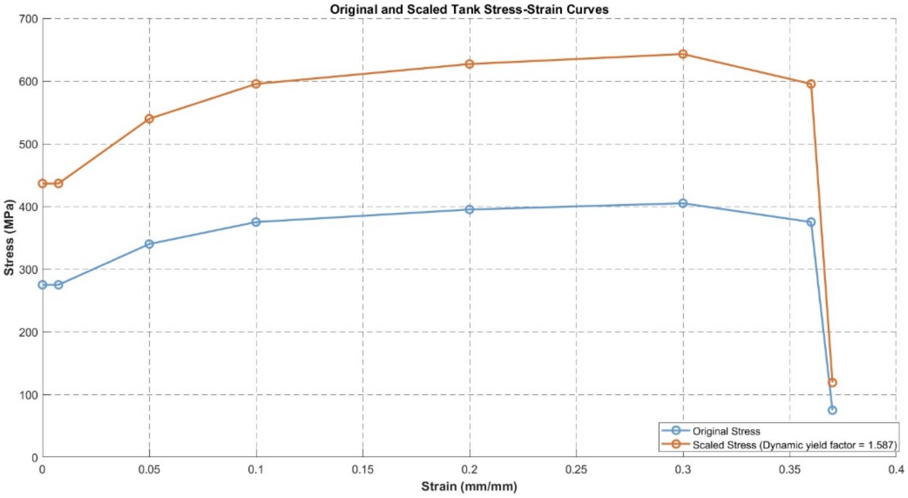

Figure 17. Stress-strain curve for steel S355 (original and scaled tank).

5 Analysis and results

This chapter will discuss the results from the NLFEA simulations performed in LS-DYNA. The effects of modeling the tank as both a rigid and a deformable body were studied. The energy absorption capacity of the GFRP grating geometries obtained from the DoE was analyzed against impact from the rigid tank and served as input for the Response Surface Methodology (RSM).

5.1 Impact scenarios

Three different impact scenarios were considered to identify the critical case that would cause the most damage to the grating and reduced energy absorption. The impact scenarios are illustrated in Figure 18.

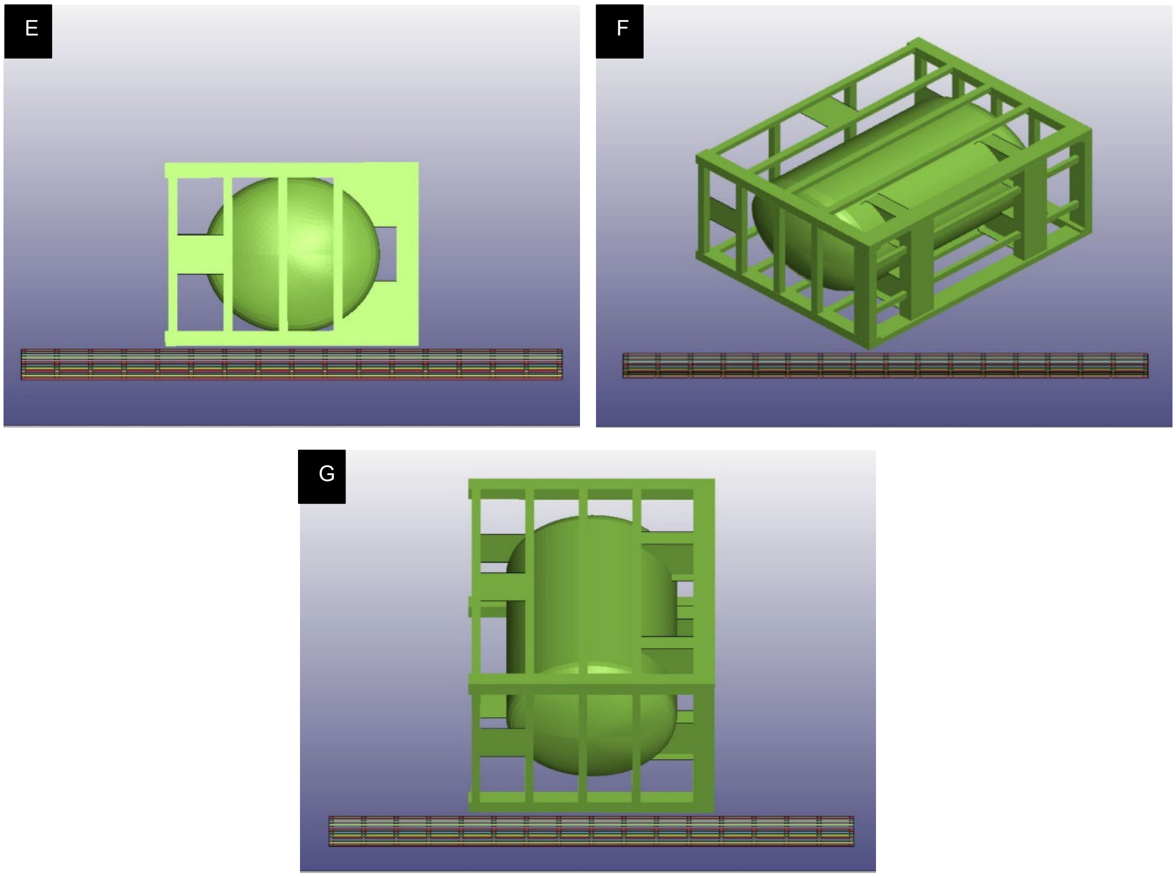

Figure 18. Impact scenarios (front view): flat (E), tip (F), side tip (G).

Impact on different locations of the GFRP grating, such as on the transversal and on the longitudinal nonintersecting ribs, was assessed to determine the most critical impact scenario. The transversal ribs experienced lower bending stress than the longitudinal ribs due to increased stiffness provided by the proximity of fixed nodes in the transverse direction.

It was found that the tank side tip impact on the longitudinal ribs was the most critical scenario when the tank is treated as a rigid body. However, when the tank is modeled as a deformable body, the critical scenario becomes the flat impact. This is further discussed in section 5.4.3.

The velocity vector of the tank was defined as normal to the grating surface to simulate the most severe impact situation [2]. The size of the grating used for this preliminary evaluation was 5x38x38 mm (WxHxP).

5.2 Rigid tank impact

5.2.1 Analysis of impact scenarios

The energy absorption capacity of the GFRP molded grating was first assessed by modeling the tank as a rigid body. The results show that the tank side tip impact scenario was the most severe, leading to an early loss of structural integrity compared to the other impact scenarios. Table 6 shows the energy absorbed by the GFRP grating after impact from the rigid tank.

Table 6. Energy absorbed by the GFRP grating in different impact scenarios with a rigid tank.

-	Side tip (Critical)	Tip	Flat
Total energy absorbed (kJ)	2.73	2.76	3.2

Therefore, all the NLFEA simulations on the geometries analyzed for the RSM were performed based on the side tip impact scenario. The results from these simulations were used to build an analytical model to predict the effect of the geometric variables of the grating on the energy absorbed. The optimization process and results are discussed in detail in section 5.3.

The boundaries for the geometric variables used to establish the design space were defined based on available grating sizes in the market and the feasibility of manufacturing non-standard sizes. The boundaries of the geometric variables of the grating are tabulated in Table 7. These boundaries are input for both the Design of Experiments and the optimization algorithm.

Table 7. Upper and lower bounds of GFRP grating geometric variables.

-	Rib Thickness (mm)	Grating thickness (mm)	Grid pitch (mm)
Upper boundary	4.4	38.0	10.0
Lower boundary	9.0	100.0	63.5

5.2.2 Design of Experiments (DoE)

The central Composite Design (CCD) method of Design of Experiments (DoE) defined the total number of experiments based on the boundaries specified in Table 7. The CCD algorithm set the number of experiments to evaluate each variable at three levels with some degree of repeatability.

Eleven different grating geometry candidates were generated for testing. Non-linear explicit dynamic simulations were performed for each geometry. Although the sample size is small, evaluating more points would have been prohibitive due to excessive computation time. The key metrics of each tested geometry are tabulated in Table 8.

Table 8. Geometries generated from the CCD.

Test No.	Rib Thickness W (mm)	Grating thickness H (mm)	Grid pitch P (mm)	Mass per unit length (kg/m)	Vf %	Energy absorbed (kJ)
1	5.3	51.3	20.8	32.4	33%	11.9
2	5.3	87.4	20.8	55.1	33%	27.8
3	8.1	51.3	20.8	43.6	22%	12.5
4	8.1	87.4	20.8	74.2	22%	32.3
5	6.7	100.7	36.8	45.7	27%	28.8
6	8.1	38	36.8	17.2	22%	3.2
7	9.0	68.4	36.8	39.1	20%	13.0
8	6.7	68.4	36.8	31.0	27%	10.2
9	5.3	51.3	52.7	14.1	33%	3.3
10	4.4	68.4	36.8	22.5	41%	7.2
11	5.0	38.0	38.0	13.3	36%	2.73

5.2.3 Strain energy

In LS-DYNA, the strain energy is labeled as the total internal energy from each deformable body. The internal energy of each GFRP molded grating after impact from the rigid tank was assessed from the NLFEA simulation results and used to model the response surface afterward (See Chapter 5.3).

None of the grating geometries tested could fully dissipate the kinetic energy from the rigid tank (99.1 kJ). All gratings experienced full penetration and loss of integrity. The interactions within the grating model are quite complex, and identifying the primary failure mode was not straightforward, especially since triaxial stresses develop as the grating resists penetration [6].

The application of a rapidly increasing dynamic load generates high strain rates and plastic stress flow [1] near the impact zone, leading to progressive damage and delamination at local spots once the GFRP grating reaches its peak resistance. The grating exhibits very brittle behavior under the impact load studied, ultimately losing its structural integrity.

Figure 19 shows the results from the test simulation of test subject number 4 (See Table 7), which has the highest energy absorption capacity among all the tested geometries. It can be noticed that 0.034 seconds after the impact, the GFRP completely lost structural integrity, collapsing around the impacted area.

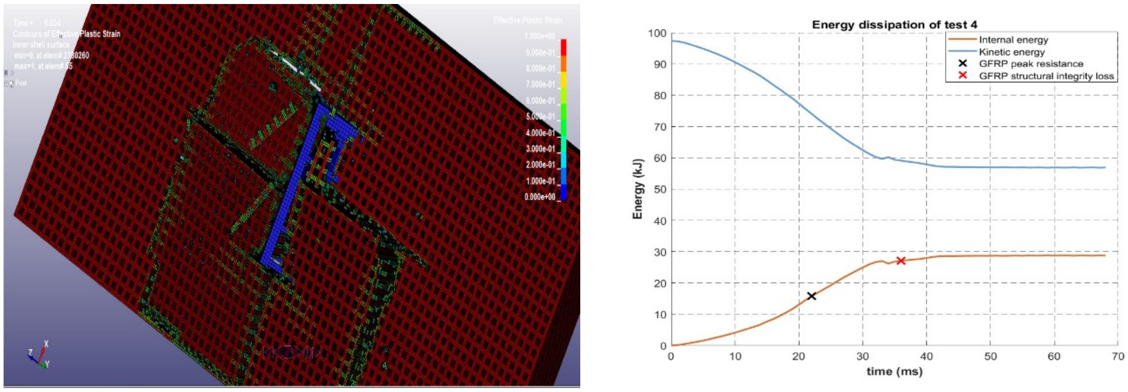

Figure 19. Grating test No. 4: effective plastic strain distribution 0.034 s after initial impact (left) and total energy absorbed (right).

Due to the premature failure of the GFRP, the total energy dissipated is lower than the grating's actual energy absorption capacity. This means that the 32.3 kJ dissipated is determined by the impact resistance against the given 99.1 kJ of the tank. For reference, the mesh metrics and solution times for this grating geometry are tabulated in Table 9.

Table 9. Mesh metrics for test grating No.4.

-	Number of elements	Number of nodes	Solution time using 8 cores (hours)
Test No. 4 (8.1x100.7x20.8)	842,409	1,156,685	96.0

5.2.4 Energy balance and hourglass

Some artificial energy was introduced to the system in the simulations, as can be noticed in Figure 20. Considering the complexity of the model, this can be attributed to instabilities when the grating and the tank are in contact. Although artificial energy is generated, the effect is negligible since it accounts for only 0.1% of the system's initial kinetic energy. Thus, it can be said that the energy balance is met.

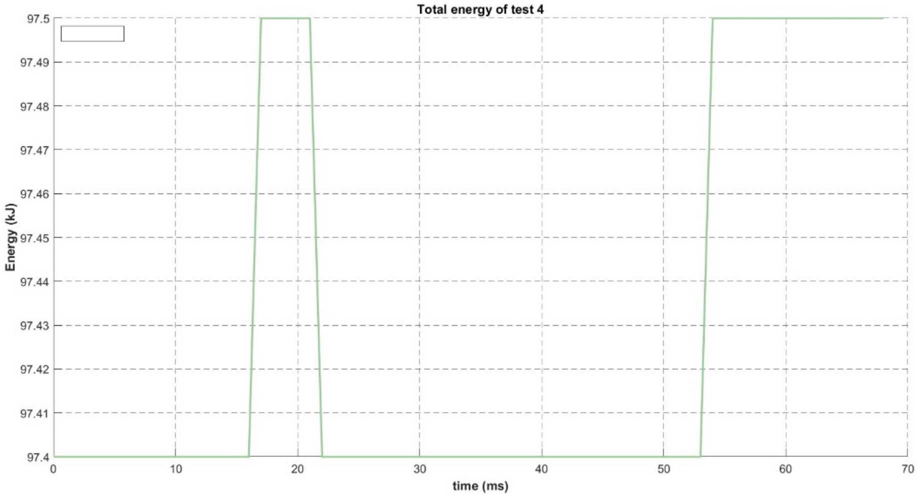

Figure 20. Rigid tank: test grating No. 4 total energy.

The complex interactions of the model and large deformations generated high hourglass energy and, in some cases, excessive reduction in solid element volume, leading to error termination. To mitigate this issue, hourglass controls were introduced to reduce hourglass energy (refer to section 4.2.3).

It was found that hourglassing depends heavily on the grating geometry, particularly on the grating thickness and grid pitch. Being the high hourglass issues particularly prevalent for gratings with thicknesses higher than 52 mm.

Although methods such as artificially increasing the stiffness of the constant stress elements were attempted, the hourglass energy exceeded 10% of the total internal energy in some simulations. Therefore, fully integrated solid elements intended for poor aspect ratios (EL - 2) were for the problematic geometries since fully integrated elements have no hourglass modes [28].

After using fully integrated elements in the challenging-to-converge simulations, it was found that the under-integrated element formulation provided a more conservative estimate of the total energy absorbed from impact, approximately 10% lower in some cases. This indicates that the grating exhibits more impact resistance and brittle behavior when modeled using fully integrated elements. However, given the high computational cost of running all the tests with fully integrated elements, this deviation was accepted.

5.3 Grating size optimization

As discussed in previous sections, the grating size influences both cost and impact resistance capacity. Therefore, there is a tradeoff between the total energy absorption capacity and the amount of material used. This chapter introduces the numerical model used to characterize the impact resistance of the geometries obtained from the DoE after performing the NLFEA simulations and the results of the size optimization on GFRP gratings.

5.3.1 Response Surface Methodology (RSM)

To generate the response surface, a numerical model that captured the interactions between the geometric variables and the total energy absorbed was necessary. Given the highly non-linear interactions and the relatively small dataset, non-linear regression models were tested to find the best fit. Second—and higher-order polynomial regression models were initially tested to describe the interactions and predict the total energy absorbed. However, these models failed to capture the complexity of the system.

It was found that the Kriging regression model provided the best fit without overfitting the data. A squared exponential kernel was used, which assumes that the behavior of the predicted variable is smooth and differentiable. The model shows a good fit of the data (See Figure 21).

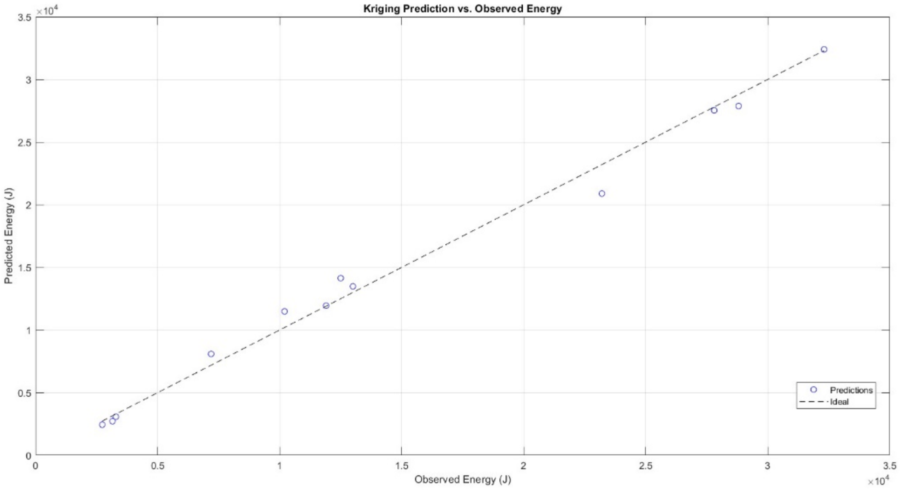

Figure 21. Goodness of fit for the Kriging model.

A k-fold cross-validation model was trained to check whether the prediction model is overfitting the data. The cross-validation evaluates how the model behaves with unseen data. The metrics of the regression model are tabulated in Table 10.

Table 10. Metrics of the regression model.

Kernel function	Squared exponential
Estimated noise level σ (J)	1887.97
k-Fold RMSE (J)	3523
Error deviation	23%

The model exhibits considerable noise, which can be attributed to the small number of samples and the complexity of estimating the energy absorbed after the structural integrity loss of the grating. The Root Mean Squared Error (RMSE) from the k-fold cross-validation indicates the expected deviation of NLFEA simulation results from the predicted absorbed energy.

This model could have been further refined by incorporating data from additional tests after analyzing the problematic zones in the response surface. However, there is a tradeoff between precision and computational costs, so the current level of precision was accepted as a first screening to explore the performance of the GFRP molded gratings.

Appendix B.4 shows the response surfaces obtained from the Kriging model. The response surfaces show that the grating thickness (H) has the highest impact on the total energy absorbed from the dropped object. This can be attributed to the increased number of reinforced layers added during the molding process to achieve higher grating thicknesses, thereby increasing flexural and shear through-thickness impact resistance.

The effect of rib thickness on the absorbed energy is surprisingly low, considering that the rib thickness (W) directly affects the fiber volume fraction of the grating in this research. The low correlation between increasing fiber volume fraction and energy absorption capacity can be attributed to the indenter impacting out of the plane of the laminae. This makes the through-thickness shear impact resistance, which is negatively affected by increasing fiber volume content, more than variations in the laminate strength. This demonstrates that although higher fiber volume fractions increase the GFRP grating's strength and flexural through-thickness impact resistance, they have a lesser effect on through-thickness shear impact resistance.

To gain a deeper understanding of how the geometric variables affect the energy absorption of a GFRP molded grating, a local sensitivity analysis was performed by assessing variations in the geometric parameters of a test grating with dimensions 6.2x36.5x 69.0 (WxHxP). From Figure 22, it can be observed that, as previously mentioned, the grating thickness clearly dominates the impact resistance and energy absorption of the grating.

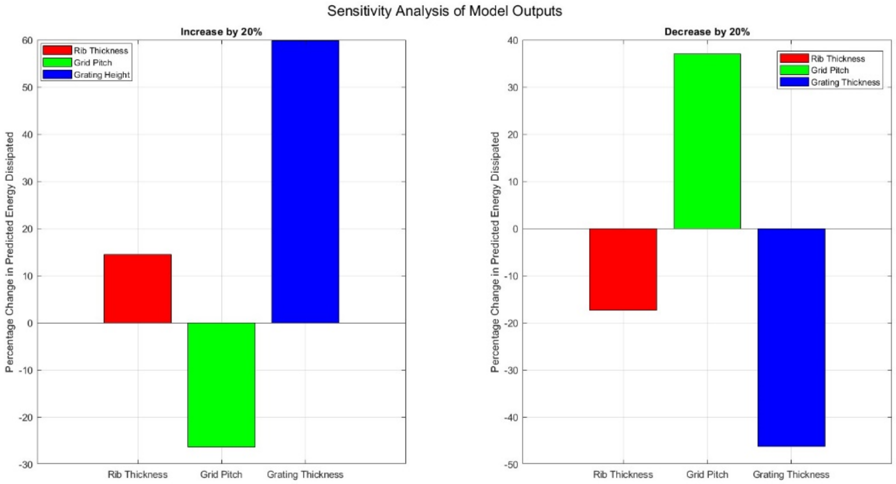

Figure 22. Sensitivity analysis of geometric variables: 20% increase (left), 20% decrease (right).

5.3.2 MOGA optimization

The three objectives imposed on the MOGA were to minimize both the weight and the total number of laminae stacked (grating thickness) while maximizing the total energy absorbed. Due to the high influence of the grating thickness on the output, the optimization model was initially biased toward selecting candidates with grating thicknesses close to 100 mm (upper bound). Hence, it was necessary to introduce penalties to the objective functions.

The outputs of the objective functions were penalized by a certain normalized percentage (%p) for geometries that violated the constraints defined in section 3.8.2 of this paper. Considerable experimentation is generally required to find a fitness function that correctly balances constraint violation terms [33]. Therefore, it was necessary to test different %p values for the objective functions. After testing several values, it was found that applying a penalty of 20% for candidates with grating thickness above 60 mm (based on the 2-inch industry standard thickness) and 10% for gratings that absorbed less than 15 kJ was appropriate.

The Pareto front surrogate model was used to generate virtual data points and identify the Pareto optimal set, representing the best tradeoffs between the objectives for the generated candidates. The population size for the MOGA was set to 500 with a maximum of 400 generations. Figure 23 shows the candidates with the best goodness of fit (colored in green).

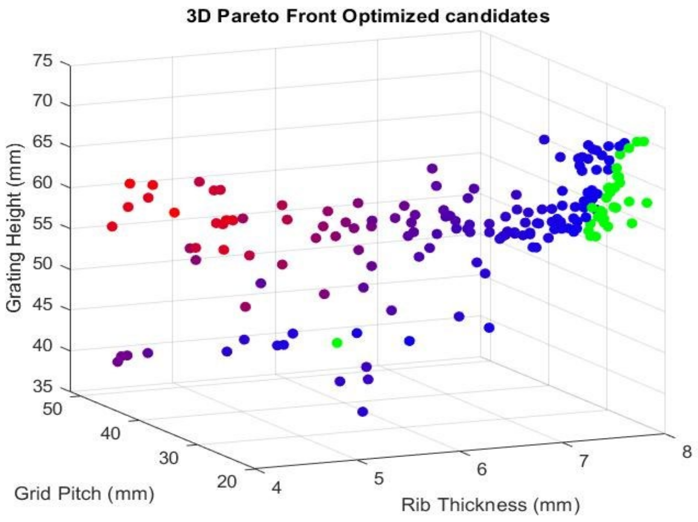

Figure 23. Mutated grating candidates after performing MOGA.

Since a penalty to the grating thickness was introduced, the best candidate population is now biased towards the upper bound of the rib thickness and the lower bound of the grid pitch. This indicates that the algorithm is being artificially forced to find a local optima instead of the global optima, which, although not ideal in other optimization problems, is acceptable given the imposed constraints on the studied model. The top 3 grating geometries based on the Pareto Front score are tabulated in Table 11.

Table 11. Top candidates obtained from the optimization model.

Rib thickness W (mm)	**Grid pitch P (mm)**	**Grating thickness H (mm)**	**Mass (kg)**	**Absorbed energy (kJ)**	**Fiber volume fraction Vf %**	**Normalized score**
7.96	22.44	62.68	49.6	18.4	22.4	1.00
7.89	23.86	59.81	44.7	16.1	22.6	0.99
7.78	22.33	63.06	49.3	18.6	23	0.98

5.3.3 Discussion on model accuracy

The dimensions of the GFRP grating geometry with the highest normalized score from the optimization were approximately 7.9x62.7x22.4 mm. This geometry was simulated in LS-DYNA to study the accuracy of the response surface. As shown in Figure 24, the total energy dissipated is approximately 22 kJ, deviating from the RSM model estimation by about 22%. This deviation aligns with the expected error from the k-fold cross-validation.

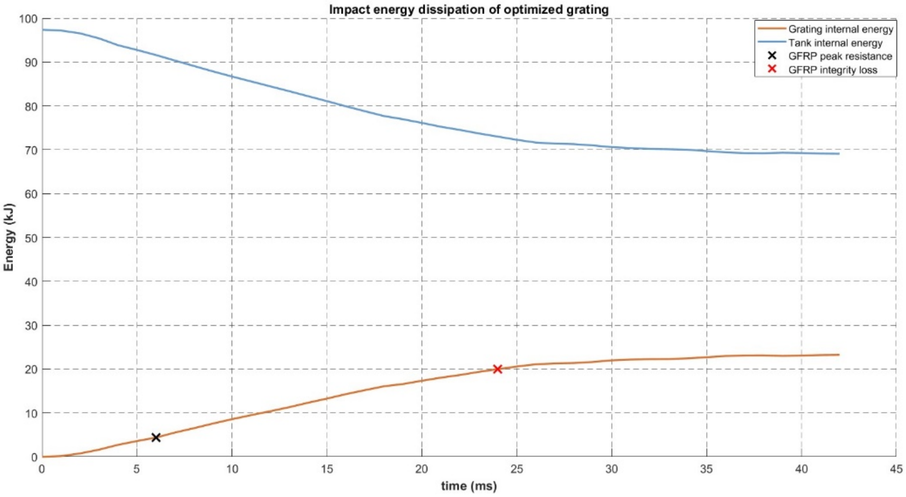

Figure 24. Total energy dissipation after impact on optimized grating geometry.

As previously mentioned, the impact load from the 99.1 kJ energy of the dropped tank exceeds the impact resistance of all the tested GFRP gratings. Consequently, the estimated absorbed energy obtained from the Kriging model does not correspond to the actual energy absorption capacity of the studied geometries.

Additionally, the structural response of the grating is highly dependent on the inertia of the dropping object. Hence, the proposed geometry might not be optimal for dropped objects with lower kinetic energies. However, this analysis provides an initial upper bound (conservative estimate) that could be used in future research.

5.4 Deformable tank impact

To study the effect of modeling the scaled tank as a deformable body on the total energy dissipation, simulations were performed using the optimum grating size obtained from the MOGA. The tank's and frame's wall thickness were scaled by a factor of 8.

Both the flat impact and the side tip impact scenarios were assessed, as the critical impact scenario varied from the rigid tank simulations. As will be further discussed in the following subsections, the tip impact scenario was not studied since the concentrated impact load caused the tank to fail before causing significant damage to the grating.

5.4.1 Flat impact

As previously discussed in section 4.3.1, the stress-strain curve was modified following the scaling laws for structural impact. However, after running the FEA simulations, it was found that the tank was behaving too stiff, causing brittle failure near the longitudinal fixed ends of the grating before the tank sustained enough plastic deformation to absorb more energy from the impact (See Appendix B.1.1). Thus, the wall thickness was further reduced to study the structural behavior under the impact of a softer tank. The initial kinetic energy remained the same for all models.

The GFRP experiences progressive damage as the tank penetrates right after the contact force reaches its peak. On the other hand, the peaks in the contact force show the damage evolution before suddenly dropping, indicating loss of structural integrity of the grating, as shown in Figure 25.

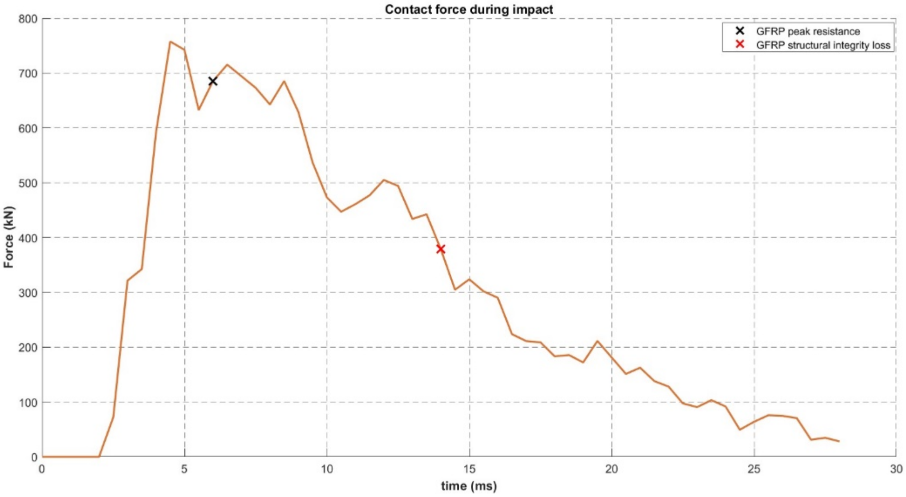

Figure 25. Deformable tank flat impact: contact force vs time.

After testing different scaling factors, it was found that downscaling the wall thickness of the tank sections by a factor of 2 (16 times lower than the original tank geometry) provided a good balance between a stiff and soft tank geometry. The total damage to the tank for both the reduced thickness (soft model) and the original scaled models is shown in Appendix B.1.

In the soft model, the grating does not fail prematurely and in such a brittle manner as the original scaled geometry. The tank undergoes large plastic deformation, causing local failure of some sections due to element erosion (plastic strain higher than 30%). Hence, the GFRP grating can absorb more energy before structural integrity loss. The total energy absorbed by each component in both models is tabulated in Table 12.

Table 12. Flat impact. total strain energy per component.

Model	**Tank strain energy (kJ)**	**Grating strain energy (kJ)**
Original scaled wall thickness	8.46	22.00
Reduced wall thickness (Soft)	11.89	23.78

As depicted in Figure 26 the grating accounts for most of the kinetic energy absorbed. With this impact configuration, the total internal energy of the system is 35.7 kJ, meaning that 36% of the initial 99.1 kJ of kinetic energy is absorbed in the form of strain energy.

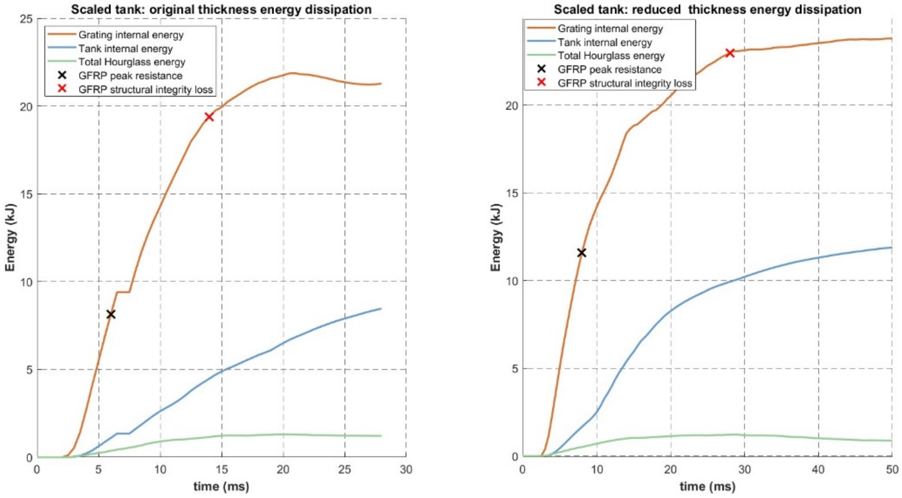

Figure 26 Total energy dissipation after impact: original scaled wall thickness (left) and reduced wall thickness (right).

5.4.2 Tip-side impact

For the tip-side impact scenario, the tank behaved very soft, experiencing large deformation and failure due to element erosion before causing significant damage to the grating (See Appendix B.2.1). Thus, the wall thickness of the tank sections had to be increased to study the effect of a stiffer tank on the energy absorption capacity of the grating.

After testing different scaling factors, it was found that scaling up the wall thickness of the tank section by a factor of 2 (4 times lower than the original tank geometry) allowed a better assessment of the energy absorption capacity of the grating. The total damage on the tank frame for both the increased thickness (stiff model) and the original scaled models can be observed in Appendix B.2. The total energy absorbed by each component in both models is tabulated in Table 13.

Table 13. Side tip impact. total strain energy per component.

Model	Tank strain energy (kJ)	Grating strain energy (kJ)
Original scaled wall thickness	38.5	14.9
Increased wall thickness	27.73	41.2

As depicted in Figure 27, the grating accounts for most of the kinetic energy absorbed. With this impact configuration, the total internal energy of the system is 68.9 kJ, meaning that 69.5% of the initial 99.1 kJ kinetic energy is absorbed in the form of strain energy.

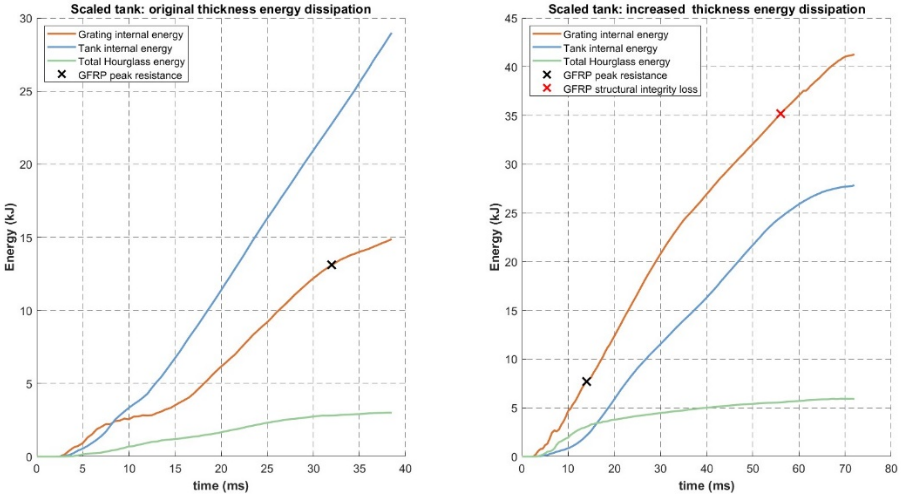

Figure 27 Total energy dissipation after impact: original scaled wall thickness (left) and increased wall thickness (right).

5.4.3 Analysis of impact scenarios

From the previous analysis, it is clear that the flat impact scenario is more critical for the deformable tank model, as it results in a stiffer behavior of the tank and rapid failure of the GFRP. On the other hand, the tip-side impact causes more damage to the tank, allowing the grating to absorb more energy before losing its structural integrity.

This difference is due to the thickness of the tank frame at the impact location and the area of the surface impacted. For the flat impact scenario, the impact load is applied over a larger area, causing a more uniform stress distribution across the frame, while for the side tip impact, the impacting section is smaller and thus sustains larger stresses, leading to excessive deformation of the tank and element erosion. The total internal energy of the system for both configurations can be observed in Figure 28.

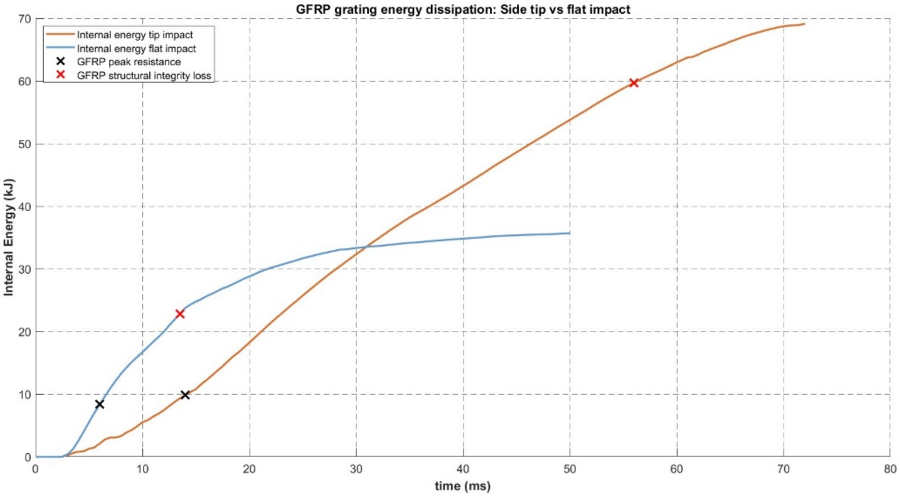

Figure 28 Comparison of deformable tank impact scenarios.

5.4.4 Energy balance and hourglass

Some artificial energy was introduced to the system, as shown in Figure 29. Considering the complexity of the model, this can be attributed to instabilities when the grating and the tank are in contact. Although artificial energy is generated, its effect is negligible since it constitutes only 0.1% of the initial kinetic energy. Thus, the energy balance is maintained. Additionally, due to large deformations and complex interactions between the tank and the grating during the impact when modeling both objects as deformable bodies, an additional element erosion criteria had to be defined for elements with a timestep lower than 1e-8 to avoid negative volume element error termination.

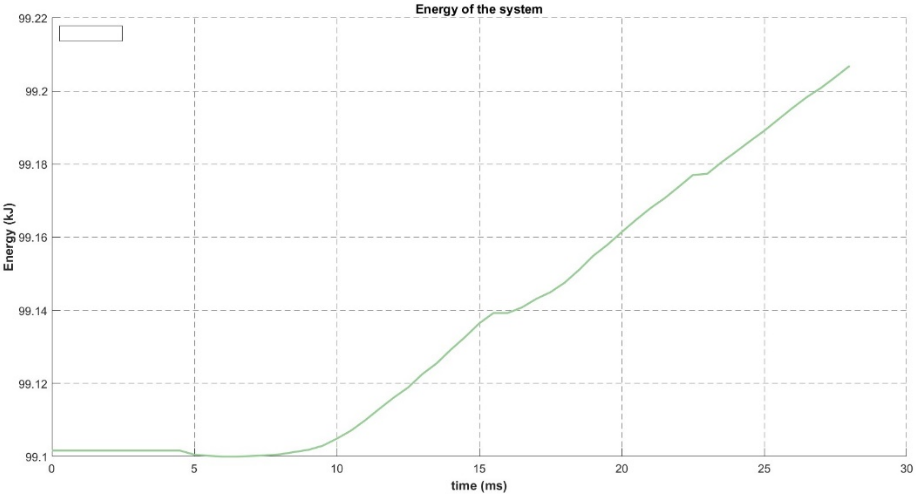

Figure 29. Deformable tank model total energy.

It is challenging to determine if the results obtained using a scaled model of the tank accurately reflect the total energy absorbed in the original system. The author believes that the original tank will absorb more energy than the scaled model, as the energy absorbed per unit volume is likely lower for the reduced geometry.

As observed in the previous simulations, the high hourglass energy issues were mitigated when modeling both objects as deformable bodies. The hourglass energy was approximately 4% of the total grating internal energy, which is within the recommended range. This improvement is likely due to a more evenly distributed local stress on the grating, as both objects are absorbing the impact energy, resulting in lower strain rates and reduced grating damage.

5.5 Additional simulations

Additional simulations were conducted to further investigate the impact energy absorption capacity of the GFRP molded grating geometry obtained from the MOGA. One of the simulations focused on a tank with a lower kinetic energy of 36 kJ, which could potentially cause significant damage to the pipeline if it were unprotected, according to the DROPS assessment. Another simulation was performed to explore the effectiveness of adding local reinforcements to the grating. The goal was to increase the total energy absorbed by combining different materials in a new substructure.

5.5.1 Energy absorption capacity

Studying the actual energy absorption capacity of the GFRP molded grating requires simulating a range of dropped objects with various kinetic energies. However, given the available resources and dropped object geometries for the present study, it was not possible to fully characterize the energy absorption capacity of the 7.9x62.7x22.4 mm grating. Nonetheless, this simulation was performed to evaluate whether the proposed GFRP grating can protect a 20-inch pipeline from dropped objects with lower kinetic energies that are still likely to cause damage and release hydrocarbons.

In this simulation, the scaled tank geometry was modeled as a rigid body, and the kinetic energy was set to 36 kJ to match that of a holding tank [6]. This experiment was performed to assess in detail whether the grating can be used for subsea protection for less demanding impact scenarios.

The simulation results show that the GFRP molded grating can effectively dissipate the energy from dropped objects with kinetic energies in the range of 36 kJ. Although the tank penetrates the GFRP grating at the impacting location, there is no integrity loss or complete failure of the grating (see Figure 30).

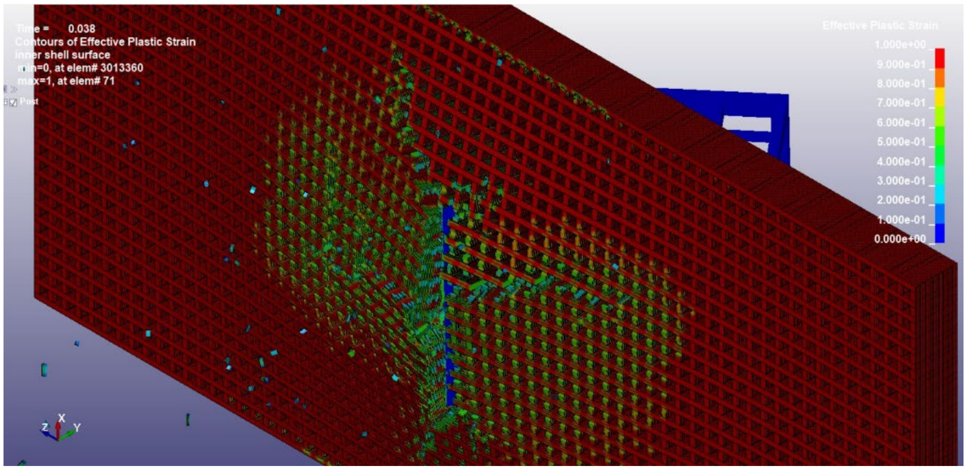

Figure 30 Effective plastic strain in GFRP upon bounce-back.

As shown in Figure 31, the tank penetrates the grating, displacing the impacted area approximately 52 mm from its original position before bouncing back, showing that the GFRP grating can protect the pipeline from dropped object impact with kinetic energy of 36 kJ.

It was deemed too expensive in terms of computational costs to continue performing simulations to determine the critical impact energy that would cause the loss of structural integrity of the grating. However, this should be assessed in future research to fully characterize the GFRP grating energy absorption capacity.

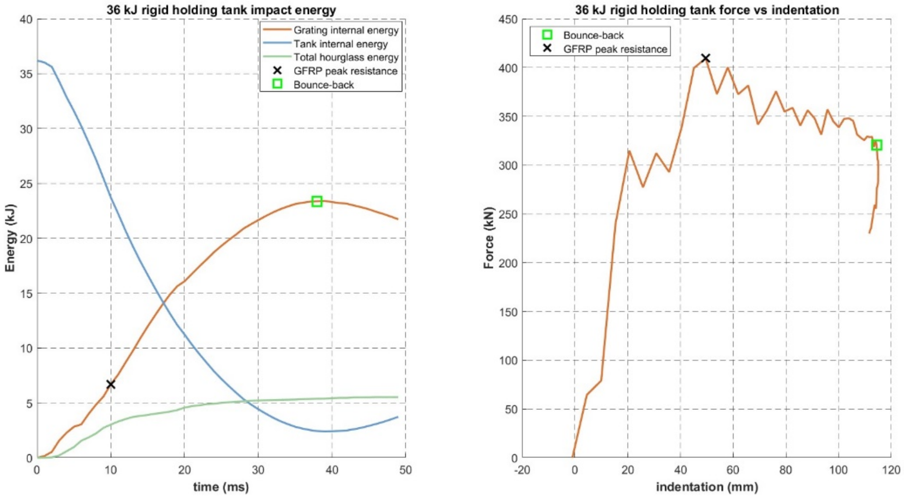

Figure 31 Rigid surge tank impact: energy dissipated (left) and force vs indentation (right).

5.5.2 Local reinforcements

As discussed in the previous section, the tank's original 99.1 kJ kinetic energy causes the grating to lose its integrity prematurely, reducing its ability to absorb energy. This issue can be mitigated by reducing the bending stresses applied to the impacted area. One way to achieve this is by adding local reinforcements forming a stiffer substructure, such as support beams underneath the GFRP molded grating. The reinforcements are proposed to be made of a material with sufficient plastic energy reserve before fracture, such as steel S355.

Therefore, to provide a reference for future research, a simple setup was created by adding three IPE80 beams (stiffeners) transversally oriented at the bottom of the grating and spaced 36 cm apart. The beams are bonded to the bottom layers of the GFRP grating. The flat impact scenario of the tank is assessed in this simulation. The tank was modeled as a deformable body using the modified stress-strain curve (refer to section 4.3.1). The longitudinal laminae located between the transversal beams were selected as the impact location.

The results of the simulation show that the beams significantly enhance the impact resistance of the GFRP molded grating by increasing its stiffness and reducing the plastic strain in areas away from the impact zone, as shown in Figure 32.

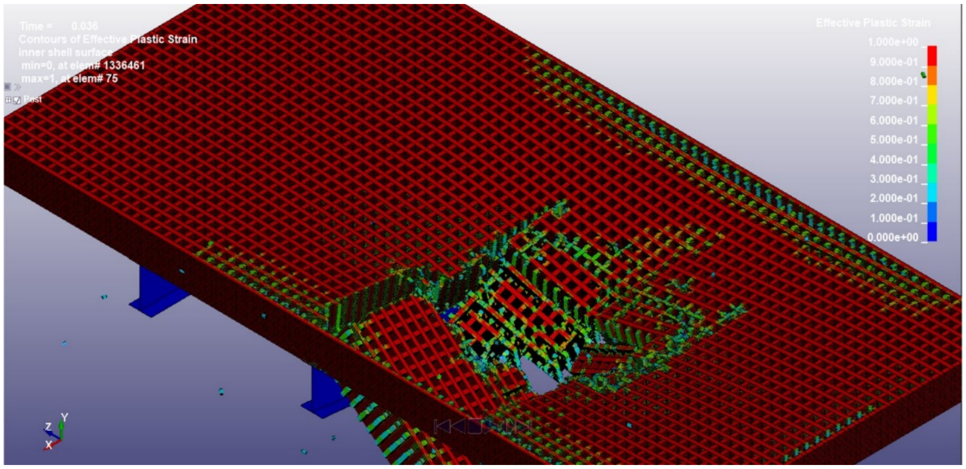

Figure 32. Effective plastic strain of the beam-reinforced GFRP molded grating.

As this configuration could not be thoroughly studied due to time constraints, the solution was stopped when the grating lost its structural integrity, and further interaction between the beams and the tank was not investigated (See appendix B.3). Although the beams only absorbed up to 9 kJ of energy, approximately 13% of the total internal energy, before the grating failed, the substructure absorbed a total of approximately 66.9 kJ. This is nearly 84% more than the energy dissipated if the beams were not included (36.44 kJ). The energy absorption curves for this simulation are shown in Figure 33.

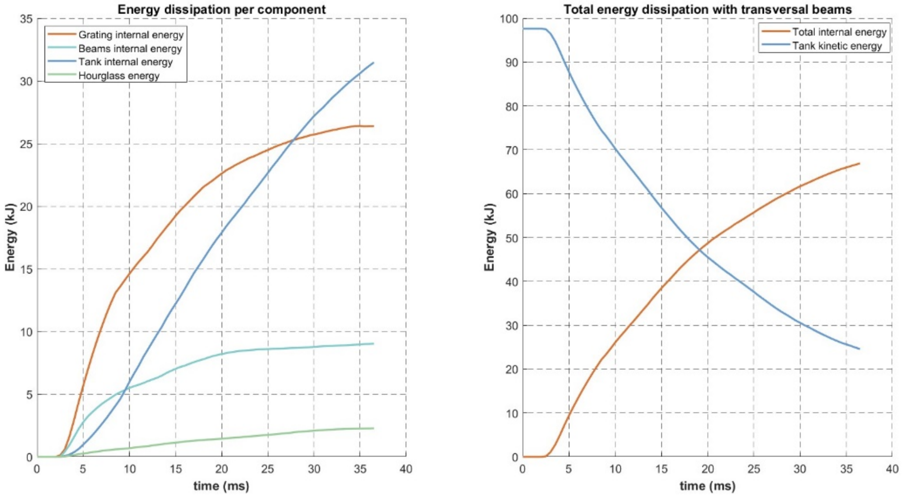

Figure 33 Internal energy component breakdown (left) and total energy dissipated (right).

Although the grating still fails before dissipating enough energy to prevent potential damage to the pipeline, the results show that combining GFRP molded gratings with steel reinforcements produces a stiffer substructure capable of absorbing more than 50 kJ of energy from the tank, meeting the DNV RP-F107 recommendations for the design of subsea pipeline protective covers.

6 Conclusion

This research provided a foundation for future studies on the energy absorption capacity of GFRP molded gratings against dropped object impact for subsea pipeline protection. The findings suggest that GFRP molded gratings can offer effective protection against impacts, depending on the kinetic energy of the dropped object.

Modeling the grating using solid elements increases the complexity of the FEA model, leading to convergence issues that require using hourglass controls and additional element erosion criteria. The hourglass modes are highly dependent on the geometry of the GFRP grating; thicknesses above 52 mm produce high hourglass energy, requiring switching to fully integrated elements to avoid this numerical issue, which increases computational costs.

The results from the Response Surface Methodology (RSM) show that the grating thickness has the most significant influence on the impact resistance and energy absorption capacity of GFRP molded gratings The Multi-Objective Genetic Algorithm (MOGA) optimization resulted in a grating with dimensions of 7.9x62.7x22.4 mm (WxHxP), offering the best tradeoff between energy absorption capacity and cost.

As stated in the peer-reviewed literature, it was found that modeling the tank as a rigid body is a conservative approach that underestimates the total energy dissipated from dropped object impact. Nonetheless, since the original tank geometry was scaled, accurately estimating the energy absorbed when both the impacting and the impacted objects are modeled as deformable bodies requires further investigation.

The structural response of the GFRP cover and its energy absorption capacity are significantly affected by the size of the indented area and the stiffness of the dropped object. Thus, when the tank was modeled as a rigid body, the side impact scenario was found to be more critical, whereas when it was modeled as a deformable object, the flat impact scenario was more severe.

Adding stiffeners to the main cover structure beneath the GFRP grating increases the stiffness of the new substructure, leading to greater energy absorption before the GFRP grating collapses. Combining GFRP gratings with steel structures demonstrated the potential to absorb more than 50 kJ from the studied dropped object, meeting DNV RP-F107 design recommendations for protective covers.

The results from the simulations have to be validated and compared with experimental data. Additionally, to study the actual total dissipated energy, the interaction between the GFRP grating and the other structural elements of the cover must be assessed using the original tank dimensions.

7 Further work and improvements

To enhance the accuracy and efficiency of future simulations, it is recommended that a model of the GFRP grating using shell elements is developed and validated against either the results from this study or experimental data. This approach will significantly decrease solution times and complexity of the model, likely mitigating the hourglass issues.

Additionally, although the proposed GFRP grating geometry fails to protect the pipeline against a 99.1 kJ dropped object kinetic energy, further NLFEA simulations are necessary to determine whether the remaining kinetic energy of the deformed tank can still cause significant damage to the pipeline, as the methodology from DNV RP-F-107 might be too conservative.

Proper engineering of the cover is essential to fulfilling the assumption of a properly constrained structure implemented in this work. A comprehensive study of the full interaction between the protective cover's primary structure and the GFRP gratings is needed to accurately assess the energy absorption capacity against a wide range of dropped objects with different kinetic energies.

Experimental testing is required to validate the results from the NLFEA simulations and fully understand the protective capacity of the proposed GFRP molded grating geometry. Additionally, modeling the effects of soil-cover interaction could provide a more realistic assessment of the total energy dissipated during dropped object impact.

.

8 References

[1] G. Lu and T. Yu, Energy absorption, Cambridge: Woodhead Publishing Limited, 2003.

[2] A. Wenger, G. Edvardsen, S. Olafsson and T. Alvestad, "Design for Impact of Dropped Objects," in *15th Annual Offshore Technology Conference*, Houston, 1983.

[3] Glassfiber Produkter AS, "Molded grating of type “heavy duty” has been tested to absorb 10 kJ blow from falling objects with a diameter of 100 mm.," Glassfiber Produkter AS, [Online]. Available: https://glassfiber.no/en/grating-subsea-protection/. [Accessed 28 May 2024].

[4] G. Xiang, K. Rao, X. Yu and X. Xia, "Overview and analysis on recent research and challenges of dropped objects in offshore engineering," *Ocean Engineering,* p. 114616, August 2023.

[5] DNV GL AS, "DNVGL-RP-F107 Risk assessment of pipeline protection," DNV GL AS, 2017.

[6] DROPS. Dropped Object Prevention Scheme, "Subsea Dropped Objects," 2010.

[7] Z. Liu, "Numerical simulation of dropped container impacts with an offshore platform deck in the North Sea," *Proceedings of the Institution of Mechanical Engineers, Part M: Journal of Engineering for the Maritime Environment,* vol. 236, no. 1, pp. 273-282, 2021.

[8] A. Ramberg, "Analysis of Dropped Objects on Offshore Installations," Norwegian University of Science and Technology (NTNU), Trondheim, 2022.

[9] Subsea Protection Systems LTD, "Concrete Mattresses," SPS Subsea Specialists, [Online]. Available: https://www.subseaprotectionsystems.co.uk/concrete-mattresses. [Accessed 1 June 2024].

[10] Allseas, "Pipeline protection," Allseas. [Online]. [Accessed 15 April 2024]. Available: https://allseas.com/activities/pipelines-and-subsea/pipeline%20protection%20/

[11] Shoretec, "Shoreblock," [Online]. Available: https://shoretec.com/wp-content/uploads/2021/01/25-Pipeline-Protection-1-Layout1.pdf. [Accessed 3 June 2024].

[12] M. A. Tauqeer and M. C. Ong, "Assessment of impact damage caused by dropped objects on Glass Reinforced Plastic (GRP) covers," in *OMAE2017-61736*, Trondheim, 2017.

[13] J. Bien, B. Hoffmesiter and M. Feldmann, "The structural behaviour of moulded gratings made of glass fibre reinforced plastics," *Composite Structures,* vol. 324, p. 117563, 2023.

[14] PJNC Ltd UK, "GRP Subsea Protection Flooring," PJNC Ltd UK, [Online]. Available: https://www.pjnc.co.uk/applications/grp-subsea-protection-flooring. [Accessed 5 May 2024].

[15] N. Gattesco, M. Dilena and I. Boem, "Experimental and numerical study on the bending performances of glass FRP molded gratings: Influence of restraining conditions and cover plates," *Elsevier,* p. 110967, 2019.

[16] DNV GL AS, "DNVGL-RP-C204 Design against accidental loads," DNV GL AS, 2017.

[17] R. Cook, D. Malkus, M. Plesha and R. Witt, Concepts and Applications of Finite Element Analysis, New York: John Wiley & Sons, Inc., 2002.

[18] K. M. Mathisen, "Solution Methods for Nonlinear Finite Element Analysis (NFEA)," Norwegian University of Science and Technology, Trondheim, 2012.

[19] E. Chatzi, G. Abbiati and K. Agathos , "The Finite Element Method for the Analysis of Non-Linear and Dynamic Systems: Non-Linear Dynamics Part I," ETH Zurich, Zurich, 2017.

[20] DNV AS, "DNV-RP-C208 Determination of Structural Capacity by Non-linear FE analysis Methods," DNV AS, 2013.

[21] ANSYS, LS-DYNA Theory Manual, LS-DYNA Dev, 2023.

[22] Advanced Micro Devices, Inc., "High-Performance Computing Explained," AMD, 2019.

[23] Sigma2/ NRIS, "Sigma2/ NRIS documentation. Fram," [Online]. Available: https://documentation.sigma2.no/hpc_machines/fram.html. [Accessed 22 April 2024].

[24] Lewis Research Center, "Simplified composite micromechanics equations for strength, fracture toughness, impact resistance and environmental effects," U.S Department of Commerce, Cleveland, 1984.

[25] Y. Sha, "CFRP strengthening of reinforced concrete pontoon walls against ship bow collisions," *Structure and Infrastructure Engineering,* vol. 18, no. 8, pp. 1091-1106, 2022.

[26] Y. Ou and D. Zhu, "Tensile behavior of glass fiber reinforced composite at different strain rates and temperatures," *Construction and Building Materials,* vol. 96, pp. 648-656, 2015.

[27] R. O. Ochola, K. Marcus, G. N. Nurick and T. Franz, "Mechanical behaviour of glass and carbon fibre reinforced composites at varying strain rates," *Composite Structures,* vol. 63, no. 3, pp. 455-467, 2004.

[28] DYNAmore Nordic AB, "Introduction to LS-DYNA," 2023.

[29] Livermore Software Technology, "LS-DYNA® Keywords User's Manual Volume I," ANSYS, Livermore, 2021.

[30] M. Reji and R. Kumar, "Response Surface Methodology (RSM): An Overview to Analyze Multivariate Data," *Indian Journal of Microbiology Research,* vol. 9, no. 4, pp. 241-248, 2023.

[31] J. Rangel, "Design optimization: Review and case study on available optimization capabilities in ANSYS," University of Stavanger, Stavanger, 2023.

[32] J. Eidsvik, "Gaussian processes: Kriging and parameter," Department of Mathematical Sciences, NTNU, Trondheim, 2019.

[33] C. D. Chapman, "Structural Topology Optimization via the Genetic Algorithm," Massachusetts Institute of Technology, Boston, 1994.

[34] T. U. Dirdal, "Dropped object impact analysis on subsea pipelines," University of Stavanger, Stavanger, 2023.

[35] M. Alves, R. E. Oshiro, M. A. G. Calle and L. M. Mazzariol, "Scaling and Structural Impact," *Procedia Engineering,,* vol. 173, p. 391–396, 2017.

9 Appendix

Appendix A: NLFEA Simulation data

Appendix A.1: Simulation workflow for dropped object impact analysis on GFRP gratings

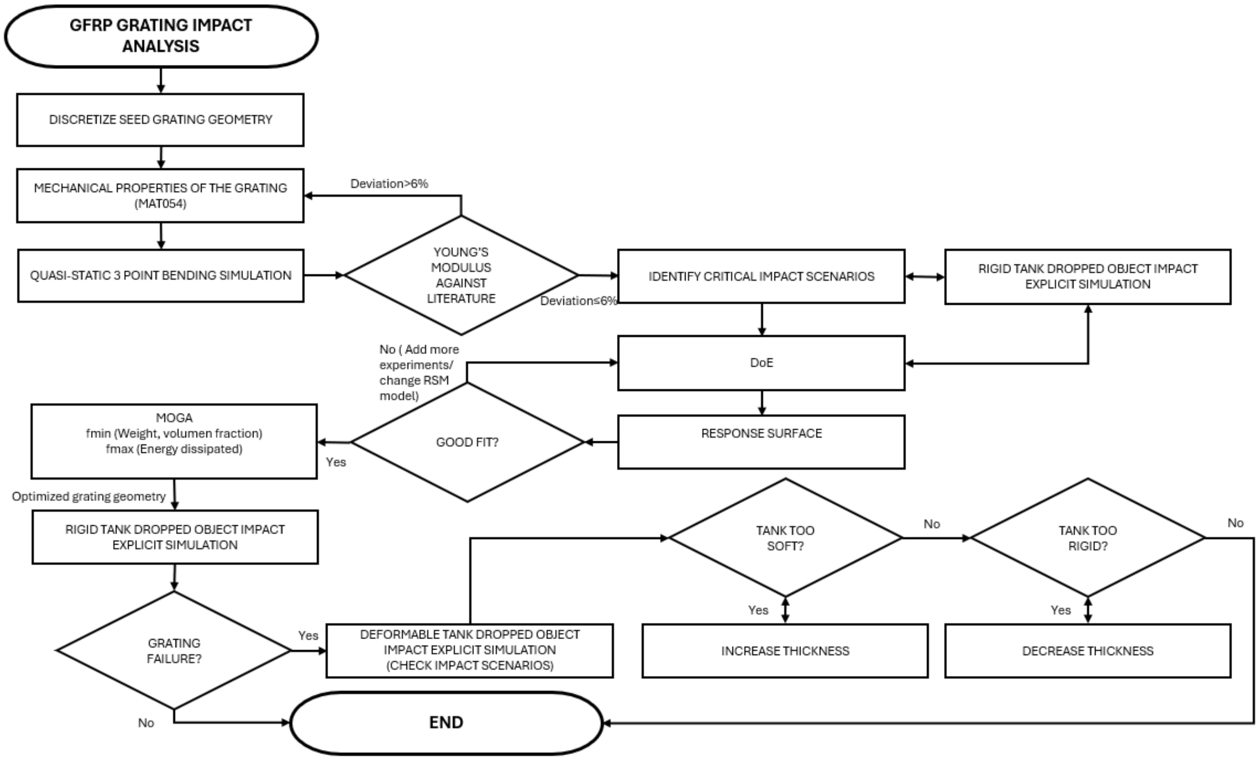

Appendix A.2: LS-DYNA material card of the molded grating reinforced laminae

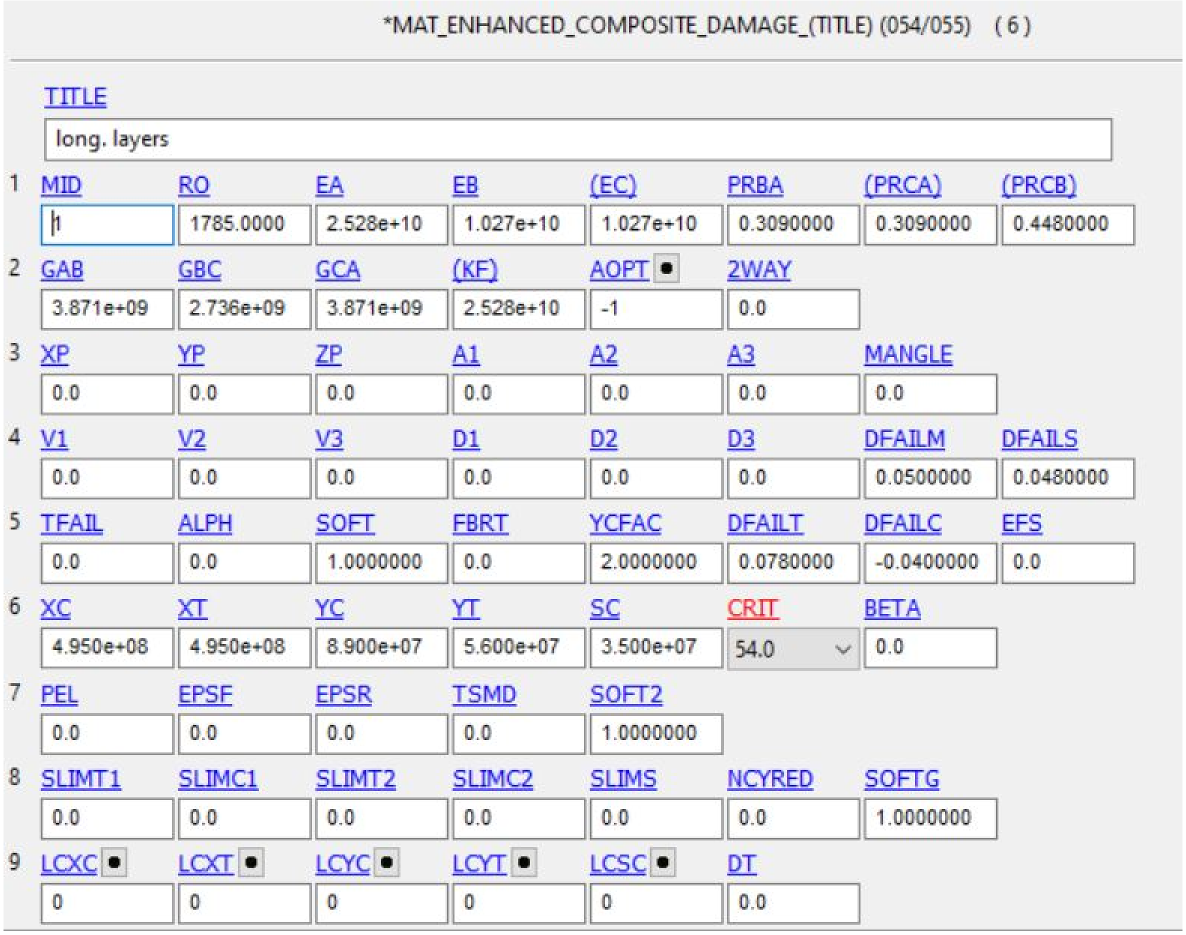

*MAT_ENHANCED_COMPOSITE_DAMAGE_(TITLE) (054/055) (6)

TITLE

long. layers

1	MID	RO	EA	EB	(EC)	PRBA	(PRCA)	(PRCB)
	1	1785.0000	2.528e+10	1.027e+10	1.027e+10	0.3090000	0.3090000	0.4480000
2	GAB	GBC	GCA	(KF)	AOPT ●	2WAY		
	3.871e+09	2.736e+09	3.871e+09	2.528e+10	-1	0.0		
3	XP	YP	ZP	A1	A2	A3	MANGLE	
	0.0	0.0	0.0	0.0	0.0	0.0	0.0	
4	V1	V2	V3	D1	D2	D3	DFAILM	DFAILS
	0.0	0.0	0.0	0.0	0.0	0.0	0.0500000	0.0480000
5	TFAIL	ALPH	SOFT	FBRT	YCFAC	DFAILT	DFAILC	EFS
	0.0	0.0	1.0000000	0.0	2.0000000	0.0780000	-0.0400000	0.0
6	XC	XT	YC	YT	SC	CRIT	BETA	
	4.950e+08	4.950e+08	8.900e+07	5.600e+07	3.500e+07	54.0	0.0	
7	PEL	EPSF	EPSR	TSMD	SOFT2			
	0.0	0.0	0.0	0.0	1.0000000			
8	SLIMT1	SLIMC1	SLIMT2	SLIMC2	SLIMS	NCYRED	SOFTG	
	0.0	0.0	0.0	0.0	0.0	0.0	1.0000000	
9	LCXC ●	LCXT ●	LCYC ●	LCYT ●	LCSC ●	DT		
	0	0	0	0	0	0.0		

Appendix A.3: LS-DYNA material card of the molded grating unreinforced laminae

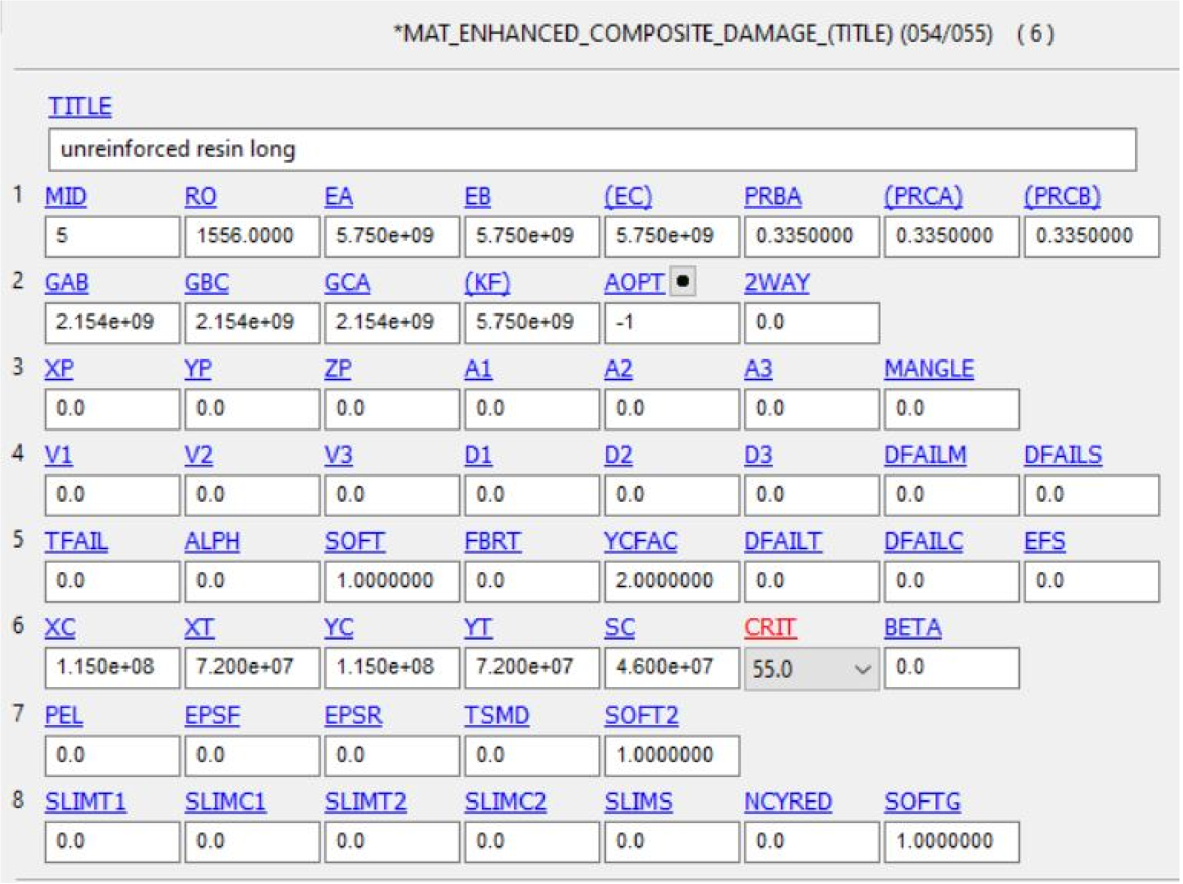

*MAT_ENHANCED_COMPOSITE_DAMAGE_(TITLE) (054/055) (6)

TITLE

unreinforced resin long

1	MID	RO	EA	EB	(EC)	PRBA	(PRCA)	(PRCB)
	5	1556.0000	5.750e+09	5.750e+09	5.750e+09	0.3350000	0.3350000	0.3350000
2	GAB	GBC	GCA	(KF)	AOPT ●	2WAY		
	2.154e+09	2.154e+09	2.154e+09	5.750e+09	-1	0.0		
3	XP	YP	ZP	A1	A2	A3	MANGLE	
	0.0	0.0	0.0	0.0	0.0	0.0	0.0	
4	V1	V2	V3	D1	D2	D3	DFAILM	DFAILS
	0.0	0.0	0.0	0.0	0.0	0.0	0.0	0.0
5	TFAIL	ALPH	SOFT	FBRT	YCFAC	DFAILT	DFAILC	EFS
	0.0	0.0	1.0000000	0.0	2.0000000	0.0	0.0	0.0
6	XC	XT	YC	YT	SC	CRIT	BETA	
	1.150e+08	7.200e+07	1.150e+08	7.200e+07	4.600e+07	55.0	0.0	
7	PEL	EPSF	EPSR	TSMD	SOFT2			
	0.0	0.0	0.0	0.0	1.0000000			
8	SLIMT1	SLIMC1	SLIMT2	SLIMC2	SLIMS	NCYRED	SOFTG	
	0.0	0.0	0.0	0.0	0.0	0.0	1.0000000	

Appendix A.4: LS-DYNA material card of steel S355 with modified dynamic yielding

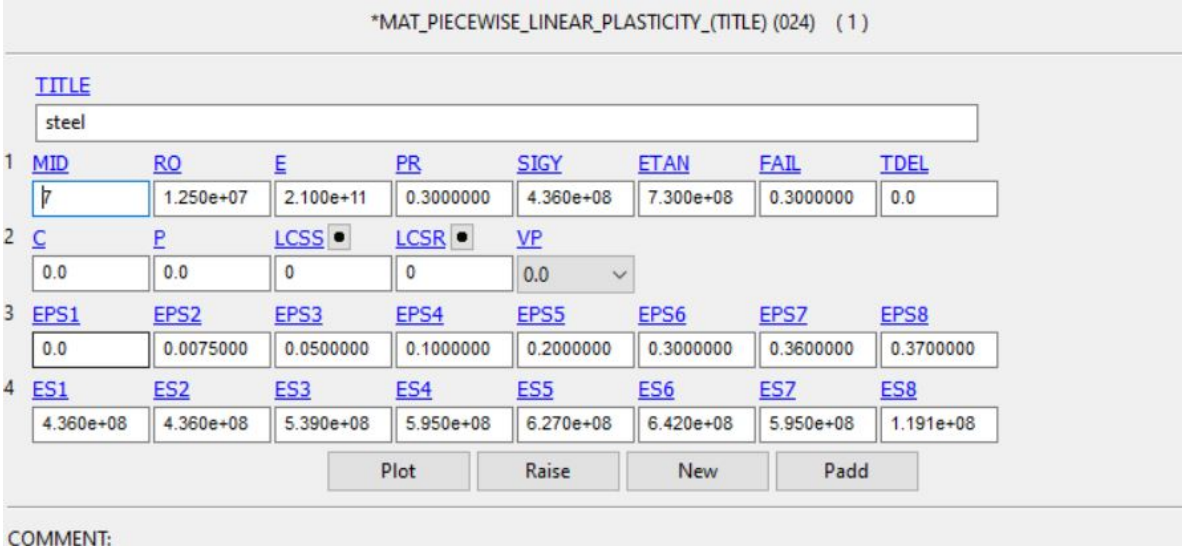

*MAT_PIECEWISE_LINEAR_PLASTICITY_(TITLE) (024) (1)

TITLE

steel

1	MID	RO	E	PR	SIGY	ETAN	FAIL	TDEL
	7	1.250e+07	2.100e+11	0.3000000	4.360e+08	7.300e+08	0.3000000	0.0
2	C	P	LCSS ●	LCSR ●	VP			
	0.0	0.0	0	0	0.0			
3	EPS1	EPS2	EPS3	EPS4	EPS5	EPS6	EPS7	EPS8
	0.0	0.0075000	0.0500000	0.1000000	0.2000000	0.3000000	0.3600000	0.3700000
4	ES1	ES2	ES3	ES4	ES5	ES6	ES7	ES8
	4.360e+08	4.360e+08	5.390e+08	5.950e+08	6.270e+08	6.420e+08	5.950e+08	1.191e+08

COMMENT:

Appendix B: Simulation Results

Appendix B.1: Deformable tank flat impact simulation

Appendix B.1.1: Original thickness. Effective plastic strain after GFRP integrity loss

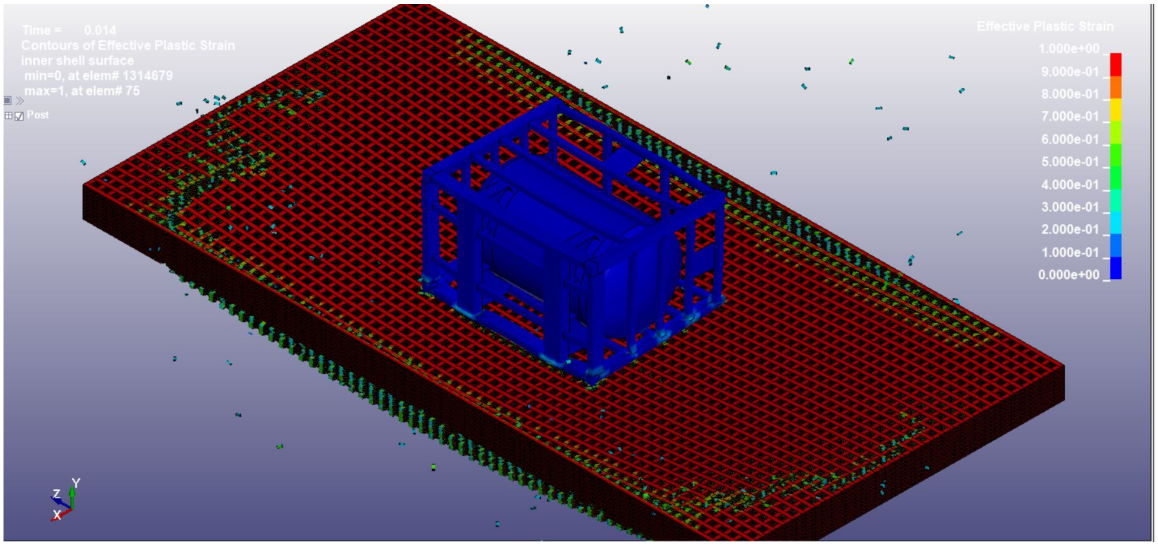

Appendix B.1.2: Original thickness. Von misses stress distribution of the scaled tank after GFRP integrity loss

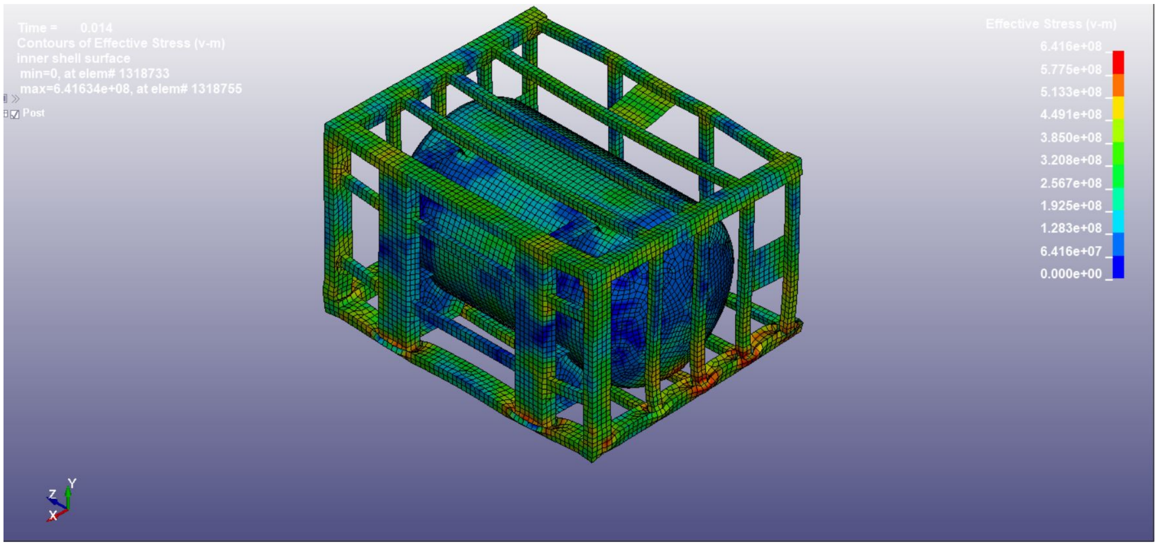

Appendix B.1.3: Reduced thickness. Von misses stress distribution of the scaled tank after GFRP integrity loss

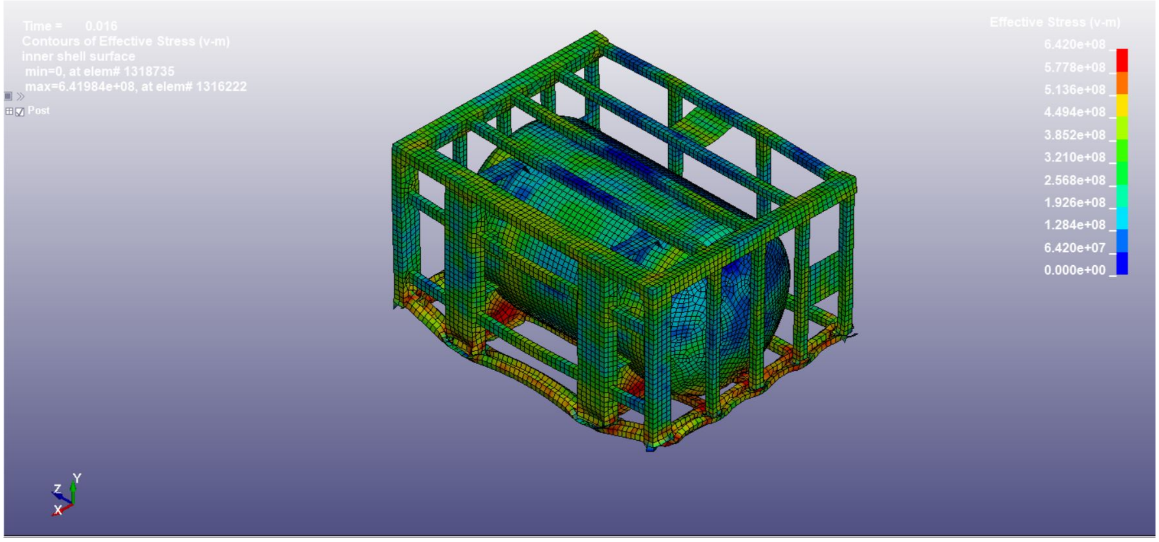

```
Time =      0.016
Contours of Effective Stress (v-m)
inner shell surface
 min=0, at elem# 1318735
 max=6.41984e+08, at elem# 1316222
```

Appendix B.2: Deformable tank tip side impact simulation

Appendix B.2.1: Original thickness. Effective plastic of the tank until progressive damage initiation in GFRP

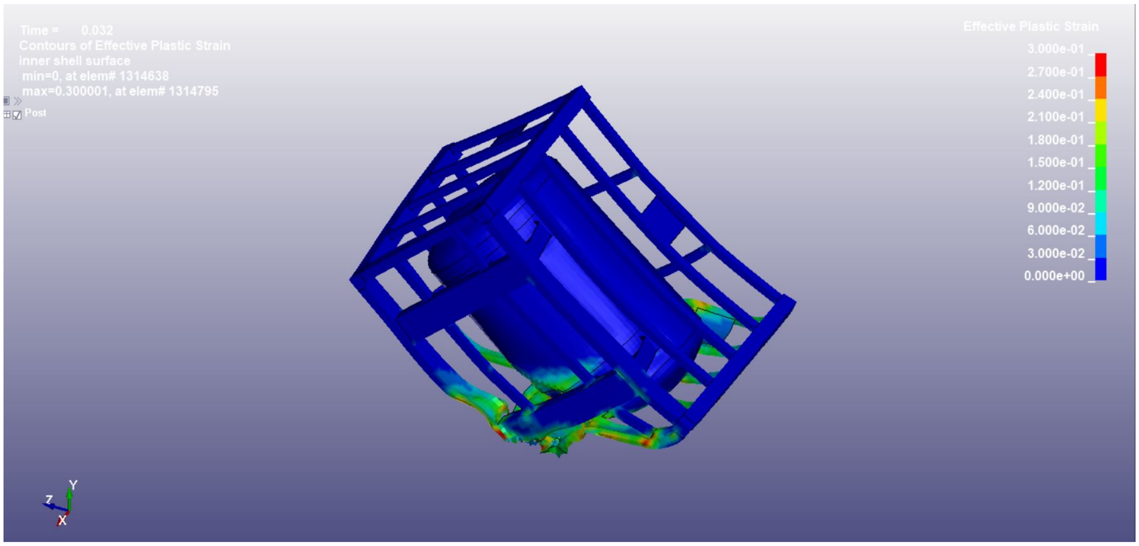

Appendix B.2.2: Original thickness. Von misses stress distribution of the tank until progressive damage initiation in GFRP

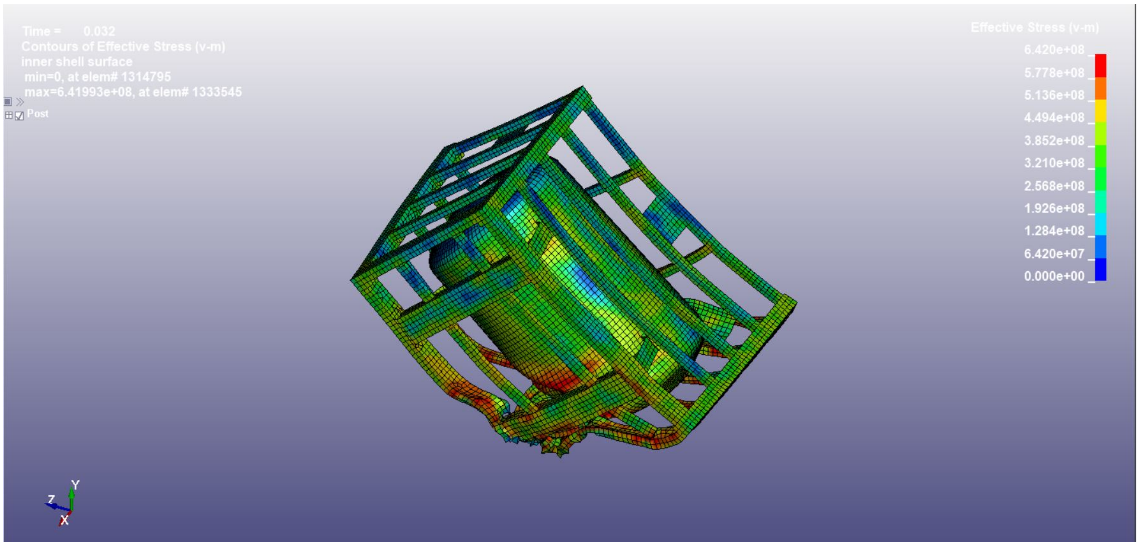

Appendix B.2.3: Increased thickness. Von misses stress distribution of the tank until progressive damage initiation in GFRP

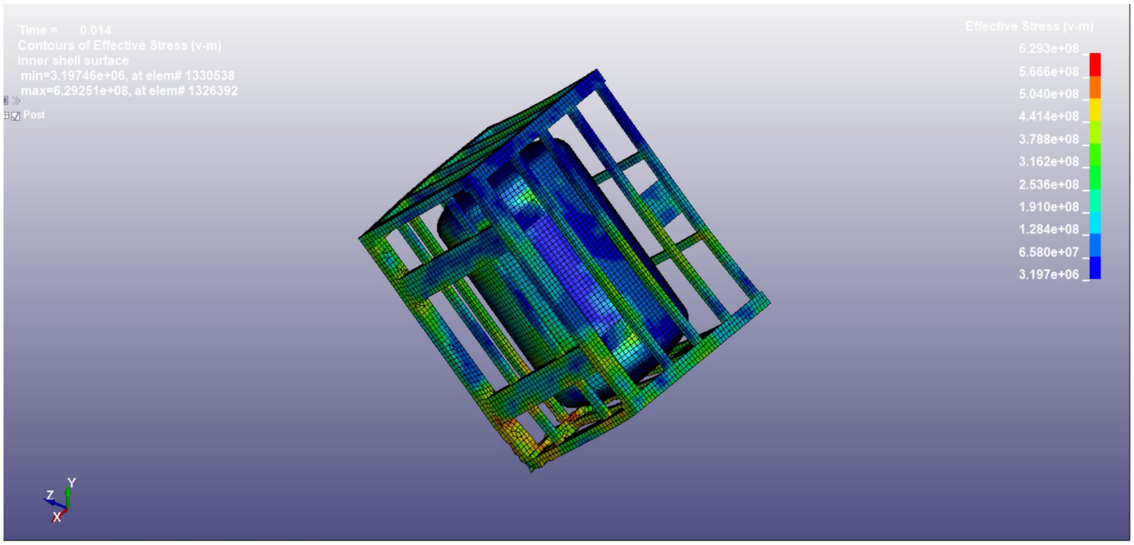

Time = 0.014
Contours of Effective Stress (v-m)
inner shell surface
min=3.19746e+06, at elem# 1330538
max=6.29251e+08, at elem# 1326392

Appendix B.2.4: Increased thickness. Von misses stress distribution of the scaled tank after GFRP integrity loss

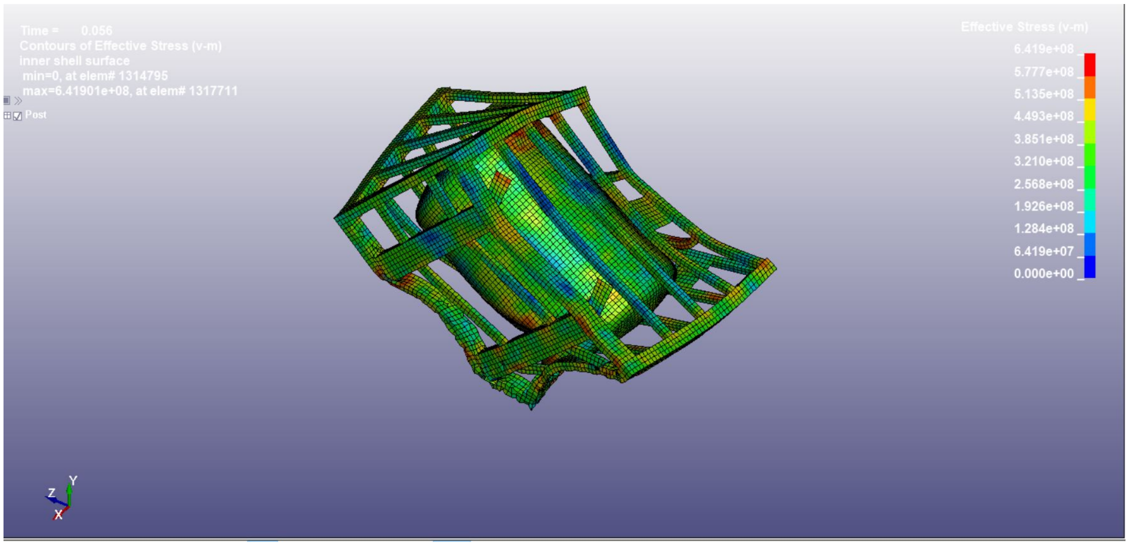

Time = 0.056
Contours of Effective Stress (v-m)
inner shell surface
min=0, at elem# 1314795
max=6.41901e+08, at elem# 1317711

Appendix B.3: Beam-reinforced grating. Von Misses stress distribution of the steel components

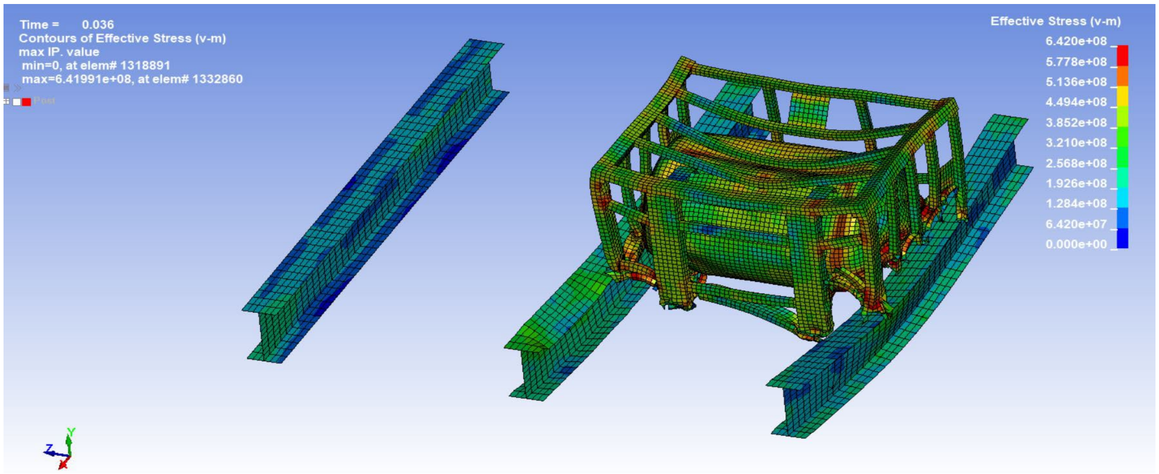

Appendix B.4: Response Surface Methodology (RSM) results.

Appendix B.4.1: Response surface - Influence of mass and fiber volume fraction.

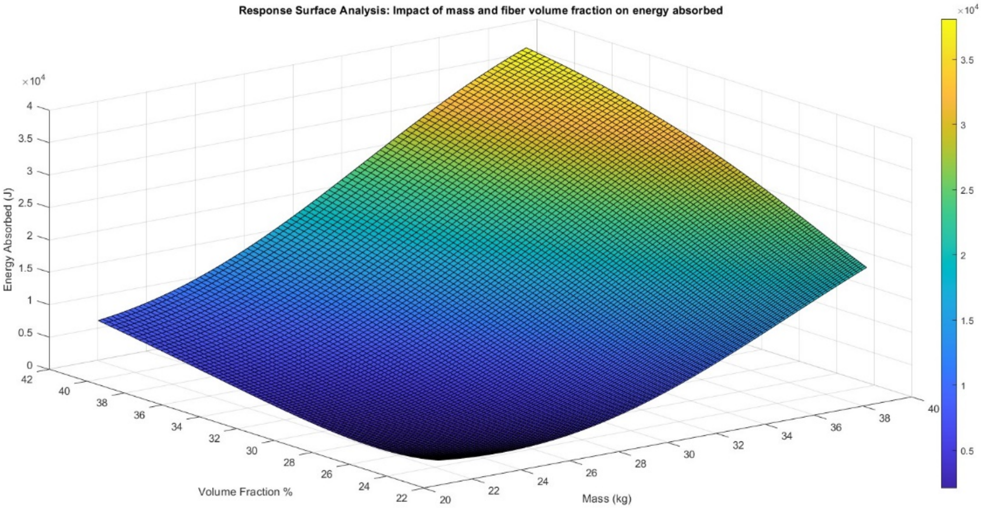

Appendix B.4.2: Response surface - Influence of grid pitch and rib thickness.

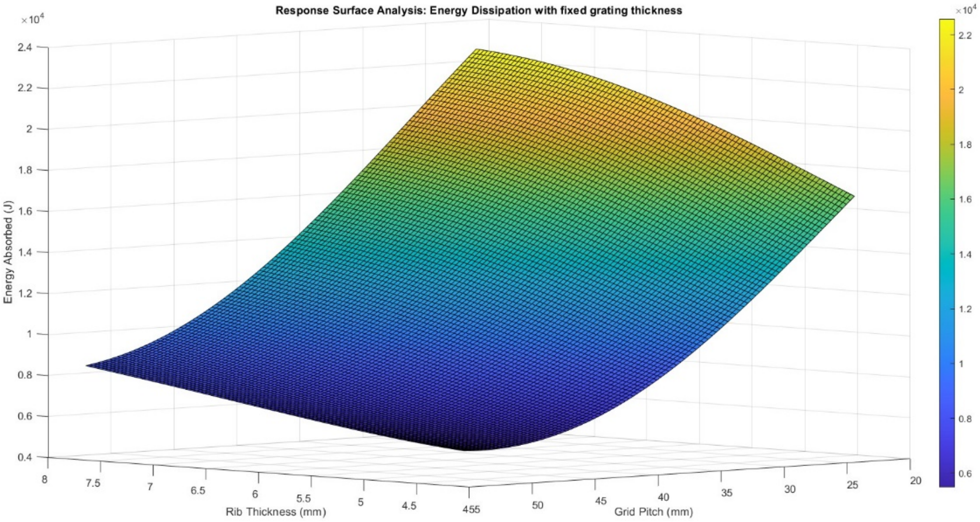

Appendix B.4.3: Response surface - Influence of grid pitch and grating thickness.